




# Robocasting of dense yttria-stabilized zirconia structures

Erwin Peng<sup>1</sup> , Xiangxia Wei<sup>1</sup>, Ulf Garbe<sup>2</sup>, Dehong Yu<sup>2</sup>, Brunet Edouard<sup>3</sup>, Aihong Liu<sup>1,4</sup>, and Jun Ding<sup>1,\*</sup>

<sup>1</sup>Department of Materials Science and Engineering, Faculty of Engineering, National University of Singapore (NUS), 9 Engineering Drive 1, Singapore 117576, Singapore

<sup>2</sup>Australian Nucl Sci and Technol Org, Bragg Inst, New Illawarra Rd, Lucas Heights, NSW 2234, Australia

<sup>3</sup>Saint Gobain Research Shanghai, Shanghai, People's Republic of China

<sup>4</sup>School of Materials and Metallurgy, Hubei Polytechnic University, Huangshi 435003, Hubei, People's Republic of China

Received: 14 April 2017

Accepted: 20 August 2017

Published online:

5 September 2017

© Springer Science+Business Media, LLC 2017

## ABSTRACT

Advanced ceramic materials with complex design have become inseparable from the current engineering applications. Due to the limitation of traditional ceramic processing, ceramic additive manufacturing (AM) which allows high degree of fabrication freedom has gained significant research interest. Among these AM techniques, low-cost robocasting technique is often considered to fabricate complex ceramic components. In this work, aqueous ceramic suspension comprising of commercial nano-sized yttria-stabilized zirconia (YSZ) powder has been developed for robocasting purpose. Both fully and partially stabilized YSZ green bodies with complex morphologies were successfully printed in ambient conditions using relatively low-solid-content ceramic suspensions (<38 vol%). The sintered structures were able to retain the original morphologies with >94% of the theoretical density despite its high linear shrinkage (up to 33%). The microstructure analysis indicated that dense fully and partially stabilized YSZ with grain size as small as  $1.40 \pm 0.53$  and  $0.38 \pm 0.10$   $\mu\text{m}$  can be obtained, respectively. The sintered partially stabilized YSZ solid and porous mesh samples (porosity of macro-pores >45%) exhibited hardness up to 13.29 GPa and flexural strengths up to  $242.8 \pm 11.4$  and  $57.3 \pm 5.2$  MPa, respectively. The aqueous-based ceramic suspension was also demonstrated to be suitable for the fabrication of large YSZ parts with good repeatability.

## Introduction

Advanced ceramic materials are highly demanded for various modern industrial and practical engineering applications because of their excellent mechanical

and physical properties [1–4]. These materials include: (1) structural ceramics such as oxide (e.g.  $\text{Al}_2\text{O}_3$ - and  $\text{Y}_2\text{O}_3$ -stabilized  $\text{ZrO}_2$ ), nitride (e.g.  $\text{Si}_3\text{N}_4$ ) and carbide (e.g. SiC) and (2) functional ceramics such as titanate (e.g.  $\text{BaTiO}_3$ ,  $\text{Pb}[\text{Zr}_x\text{Ti}_{1-x}]\text{O}_3$ ), ferrite (e.g.  $\text{NiZnFe}_2\text{O}_4$ ,

Address correspondence to E-mail: msedingj@nus.edu.sg

CoFe<sub>2</sub>O<sub>4</sub>) and oxide superconductor (e.g, YBCO) [5–12]. Of various advanced ceramics materials, yttria-doped zirconium oxide (YSZ) material is particularly of interest due to its wide range of applications [6, 13, 14]. With 3 mol % yttria dopant, tetragonal polycrystalline or partially stabilized YSZ structure is expected to possess excellent mechanical properties due to transformation toughening mechanism [15]. At yttria doping content above 5 mol %, cubic YSZ structure is expected to have good ionic conductivity that is suitable as ceramic oxygen ion conductors or solid electrolyte [16]. With the increasing demand for ceramic parts with intricate morphologies, traditional ceramic processing methods (e.g, casting and moulding) were no longer adequate [17–19]. To overcome this issue, ceramic additive manufacturing (AM) technology which allows for a high degree of fabrication freedom has been gaining significant interest [20–22]. The current ceramic AM techniques include: (1) selective laser sintering (SLS) [23], (2) powder bed fusion (i.e, binder Jetting) [24], (3) micro-stereolithography (CμSL) [25], (4) fused deposition of ceramics (FDC) [26] and (5) robocasting or extrusion free forming (EFF) [20, 27]. Among these techniques, robocasting that relied on computer-controlled robotic deposition of highly dispersed colloidal ceramic suspensions through a small orifice to form three-dimensional structure was often considered due to its simple process, low-cost and the flexibility to print a wide variety of ceramic materials [7, 8, 10, 11, 20, 27, 28].

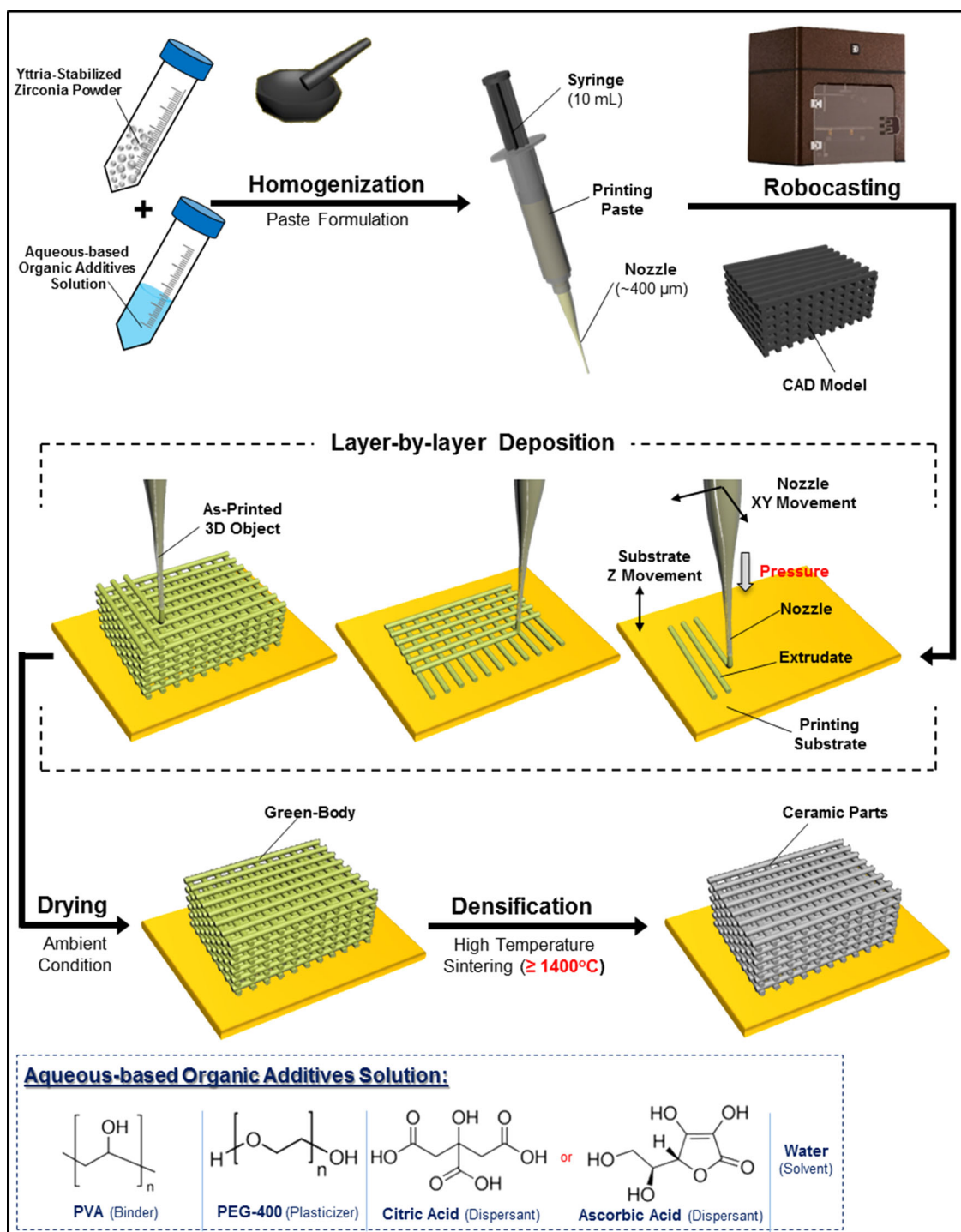
In robocasting, obtaining high-quality ceramic parts relies on the successful strategy to overcome shrinkage problem which usually caused severe cracks development and sample deformation [20, 21]. To date, different strategies have been proposed to obtain good ceramic parts through robocasting by tackling the shrinkage problem. (1) The classical strategy was to increase the ceramic solid loading content as high as possible [21, 29–31]. While the sample shrinkage can be minimized, high-solid loading ceramic suspension was prone to agglomeration which can severely cause nozzle clogging during extrusion process. (2) Alternatively, freeze-form extrusion fabrication technique which relied on immediate freeze of the printed green body to preserve the printed structure was proposed previously [32]. (3) Robocasting with UV-curable ceramic suspensions followed by post-printing polymerization to obtain hardened green body has also been reported

[33, 34]. Despite its effectiveness to prevent sample deformation, both freeze-form route and UV curing process were considered a tedious and slow process. It also required complicated setup or printing environment (due to the need of either cooling system or in situ UV curing apparatus). The addition of UV-curable binder also increased the complexity during the binder burnout process. (4) Robocasting with ceramic suspensions dispersed in hydrogels was considered [35]. The gelling of hydrogel after printing enabled shape retention; however, additional temperature control was required to ensure proper gelling condition. (5) Robocasting with solvent-based ceramic suspensions has also been reported previously [36, 37]. The use of organic-solvent enabled green body quick drying due to fast evaporation of the toxic or volatile solvent. Such process is dangerous, especially when printing larger parts due to the large amount of solvent evaporation. Aqueous ceramic suspension was usually preferred over the solvent-based system due to its low cost, simple handling, low toxicity and slower drying process [38]. (6) Lastly, to promote a better control over drying process and sample shrinkage, robocasting in oil bath has been demonstrated [20, 35, 39]. While such strategy was useful to fabricate porous structures, printing dense part within oil bath often caused oil trapping between the deposited extrudates, leaving periodic defect or cavity after drying and sintering. Although different robocasting strategies have been demonstrated for fabricating ceramic parts, it still remained challenging to fabricate high-quality dense ceramic parts by robocasting in just a few steps process.

In this paper, aqueous-based ceramic suspensions comprising of commercial nano-sized yttria-stabilized zirconia (denoted as YSZ) powders with low solid loading content (up to 38 vol%) were developed and used for robocasting fabrication of ceramic green body. Following the post-printing high-temperature pressure-less sintering process, the as-fabricated YSZ ceramic green bodies were sintered into the dense and high-quality YSZ parts. To keep the overall process simple and cost-effective, five synergistic strategies were considered: (1) Robocasting was carried out using commercially available fused deposition modelling (FDM) 3D printers equipped with universal paste extruder (approx. USD 3500.00); (2) low-solid loading ceramic suspensions were used to avoid the use of high-energy ball milling process in

preparing the ceramic suspensions (see Scheme 1); (3) deformation/cracks development due to excessive shrinkage of the low-solid loading green body during drying process was mitigated by employing a

controlled shrinkage approach. The printing substrate was coated with non-toxic releasing agent (e.g. oleic acid) in order to release the strain between the printed green body and substrate (see ESI Figure S2



**Scheme 1** Schematic diagram illustrating the (1) YSZ suspensions preparation, (2) bulk YSZ structures robocasting to obtain green body with complex morphology and (3) post-printing densification process to obtain YSZ parts.

for more details). This allows the sample to shrink uniformly during drying process, resulting in the increase in the green body density during drying stage. (4) Commercial YSZ nano-sized powders with high specific surface area (Saint Gobain ZirPro; <60USD per kg) with good sinterability were employed. By appropriately choosing YSZ powders with high specific surface area, relatively low sintering temperature to yield dense YSZ structure down to 1400 °C can be achieved; lastly, (5) inexpensive and non-toxic organic additives were used to disperse the ceramic powders in water. By avoiding the use of volatile, toxic or flammable solvent (e.g. methyl ethyl ketone, ethanol, toluene and  $\alpha$ -terpineol) [27, 37]. The overall ceramic paste preparations can be accomplished in an open bench without the need for ventilated fumehood environment. Microstructure analysis, crystal structure analysis and simple mechanical testing were performed on the sintered bulk YSZ parts. The developed aqueous-based YSZ ceramic suspensions were also demonstrated to be suitable for printing large YSZ ceramic parts with good repeatability.

## Experimental procedure

### Materials

High-purity YSZ powders: CY6Z-NA, CY3Z-NA and CY3Z-P were kindly provided by Saint Gobain (ZirPro). Organic additives such as polyvinyl alcohol (PVA;  $M_w$  31000) binder, poly (ethylene glycol) (PEG-400;  $M_n$  400) plasticizer as well as L-ascorbic acid (AA) and citric acid (CA) dispersant were purchased from Sigma-Aldrich (Singapore). Deionized water was used as solvent to dissolve the binder and dispersant. Binder solution containing 12.5 wt% of PVA and dispersant solution (AA or CA; 200 mg mL<sup>-1</sup>) were prepared beforehand.

### YSZ ceramic suspensions preparation

The aqueous ceramic suspensions containing commercial YSZ powder were prepared by homogenizing YSZ dry powder with appropriate amount of organic additives (mixture of dispersant, plasticizer and binder in water). Approximately, the 0.2–0.5 wt% dispersant, 0.35–0.5 wt% binder and 0.25 wt% plasticizer on a dry weight bases (dwb)

against the YSZ powder amount were added. Due to their surface chemistry differences, AA dispersant was used for CY3Z-P while CA dispersant was added for CY6Z-NA and CY3Z-NA. The resultant mixture was homogenized thoroughly in an agate mortar using pestle for at least 15 min to (1) allow YSZ powders de-agglomeration, (2) allow uniform mixing and (3) evaporate significant amount of water to form a thick suspensions. To avoid any further water evaporation, the resultant suspensions were immediately transferred into the 10- or 20-mL disposable plastic syringe equipped with tapered plastic nozzle (22G; 410  $\mu$ m diameter). A gentle taping of the syringe to table/hard surface while pushing the plunger may help to minimize the trapped air bubbles.

### Robocasting of YSZ ceramic suspensions

Low-cost commercial FDM printer 3Dison Multi (South Korea) equipped with universal extruder system (ROKIT Inc.) was used. The STL files were prepared using Autodesk® 3DsMax. CreatorK® software was used to prepare the STL file for the printing (with 100% infill setting; 400–600- $\mu$ m layer height/thickness; 1.45 width over height ratio for solid samples and 1–1.2 width over height ratio for porous/mesh samples; 5–40 mm s<sup>-1</sup> printing speed/feeding rate). The width over height ratio for solid samples determined the centre-to-centre distance between the extruded filaments. Following Scheme 1a, the ceramic suspension was extruded onto acrylic substrate pre-coated with releasing agent (i.e. oleic acid). Tapered nozzle (22G), which allowed lower printing pressure as compared to cylindrical tip, was used during the printing. All samples were printed at ambient condition. The as-printed green body was allowed to dry slowly at ambient temperature for 12 h in order to prevent any unnecessary drying cracks and deformation due to sudden solvent evaporation.

### Post-printing debinding and sintering

For the post-printing densification treatment, the dried green body was sintered using Carbolite HTF 18/4 box furnace (UK). Following the TGA results, the debinding process was carried out at 600 °C for 1–2 h. Following the debinding process, the samples were sintered at  $\geq 1400$  °C for either 5, 10 or 20 h with a constant heating rate of 1 °C min<sup>-1</sup>. After the



sintering, the samples were allowed to naturally cool to room temperature.

### Materials characterization

The YSZ powders were analysed for its hydrodynamic size distribution and zeta potentials by using Malvern Zetasizer Nano-ZS (Worcestershire, UK). The powders were dispersed in water and sonicated for 10 min prior to the measurement. The desired pH during the measurement was achieved by adjusting the solution pH with HCl or NaOH solutions. Ceramic suspension rheological measurements were performed on TA Instruments DHR-2 rheometer using 40-mm-diameter parallel plates at 800- $\mu\text{m}$  measurement gap. The apparent viscosity of the suspensions was measured at 25 °C in a shear rate sweep mode (flow ramps) with shear rate ranging from 0.01 up to 200  $\text{s}^{-1}$ . The dynamic mechanical analysis (DMA) was carried out at 1-Hz frequency by varying the oscillation stress from 0.1 up to 2000 Pa. The yield stresses ( $\tau_y$ ) were determined at which the storage modulus ( $G'$ ) is equal to the loss modulus ( $G''$ ). The paste flow properties can be approximated by using Herschel–Buckley model  $\tau \approx \tau_y + K\dot{\gamma}^n$ , where  $K$  is the viscosity parameter (flow consistency index) and  $n$  is the flow behaviour index or shear thinning coefficient [35, 39]. Both  $K$  and  $n$  were determined from the fitting of  $\log(\tau - \tau_y) = \log(K) + n \cdot \log(\dot{\gamma})$ . The inorganic YSZ content in the ceramic suspensions was analysed by TA Instruments SDT Q600. The ceramic suspensions containing CY6Z-NA/CY3Z-P were heated to 1000 °C in air environment, and the weight lost was recorded.

The microstructures of the YSZ powders and the sintered samples were observed directly under scanning electron microscope (SEM) with 5-kV acceleration voltage (Zeiss; FESEM Supra 40) without any grinding/polishing. The elemental mapping analysis was performed using energy-dispersive X-ray spectroscopy (EDX) attached to the SEM. The YSZ powders and the sintered samples were examined by X-ray diffractometer (XRD; Bruker D8 Advanced Diffractometer system) with Cu K $\alpha$  source (1.5418 Å). The X-ray photoelectron spectroscopy (XPS) spectra of the sintered samples were taken using an Axis Ultra DLD X-ray photoelectron spectrophotometer equipped with an Al K $\alpha$  X-ray source (1486.69 eV). The energy step size of the XPS was 1 eV for the survey scans and 0.1 eV for the fine

scans. The subtraction of the Shirley background composition analysis and the XPS peaks deconvolution were carried out by using Casa XPS (2.3.14 version). The XPS spectra were calibrated to the  $\text{sp}^2$  hybridized carbon peak at 284.6 eV. The neutron imaging measurements were carried out at the neutron radiography instrument DINGO (see Figure S19 for more details) at the OPAL research reactor (Sydney, Australia) [40]. The measurement protocols can be found in ESI Section S6.

### Density measurement and mechanical testing

The sintered samples hardness test and the flexural strength measurement were carried out using (1) Indentec Vickers hardness testing machines (Zwick/Roell) using 5kgf load (HV05) and (2) Lloyd LR10 K plus universal testing machine (Ametek, USA) equipped with three-point bending test fixture. The density of the sintered YSZ structures was determined by Archimedes method using Matsumoku electronic densimeter.

## Results and discussion

### Commercial powder precursors characterizations

In this work, three different commercial nano-sized YSZ in granular forms were employed as the starting precursors: (1) CY6Z-NA, (2) CY3Z-NA and (3) CY3Z-P (Saint Gobain ZirPro, Shanghai). The respective powders compositions are summarized in Table S1 (ESI). The CY6Z-NA powders comprised of 6 mol % yttria while both CY3Z-NA and CY3Z-P powders contained 3 mol % yttria content. The specific surface area for both CY6Z-NA and CY3Z-NA powders (at 7.0  $\text{m}^2 \text{g}^{-1}$ ) were lower than CY3Z-P powder (at 9.0  $\text{m}^2 \text{g}^{-1}$ ). These powders were dispersed in water by sonication and examined prior to the ceramic powder processing. From the SEM images of CY6Z-NA, CY3Z-NA and CY3Z-P (in Fig. 1a–c), all YSZ powders were irregular in shape with average particle size of less than 500 nm. When examined by DLS experiment, the dispersed YSZ powders in water showed uniform size distributions, as indicated in Fig. 1d. The average hydrodynamic size of CY6Z-NA, CY3Z-NA and CY3Z-P particles in

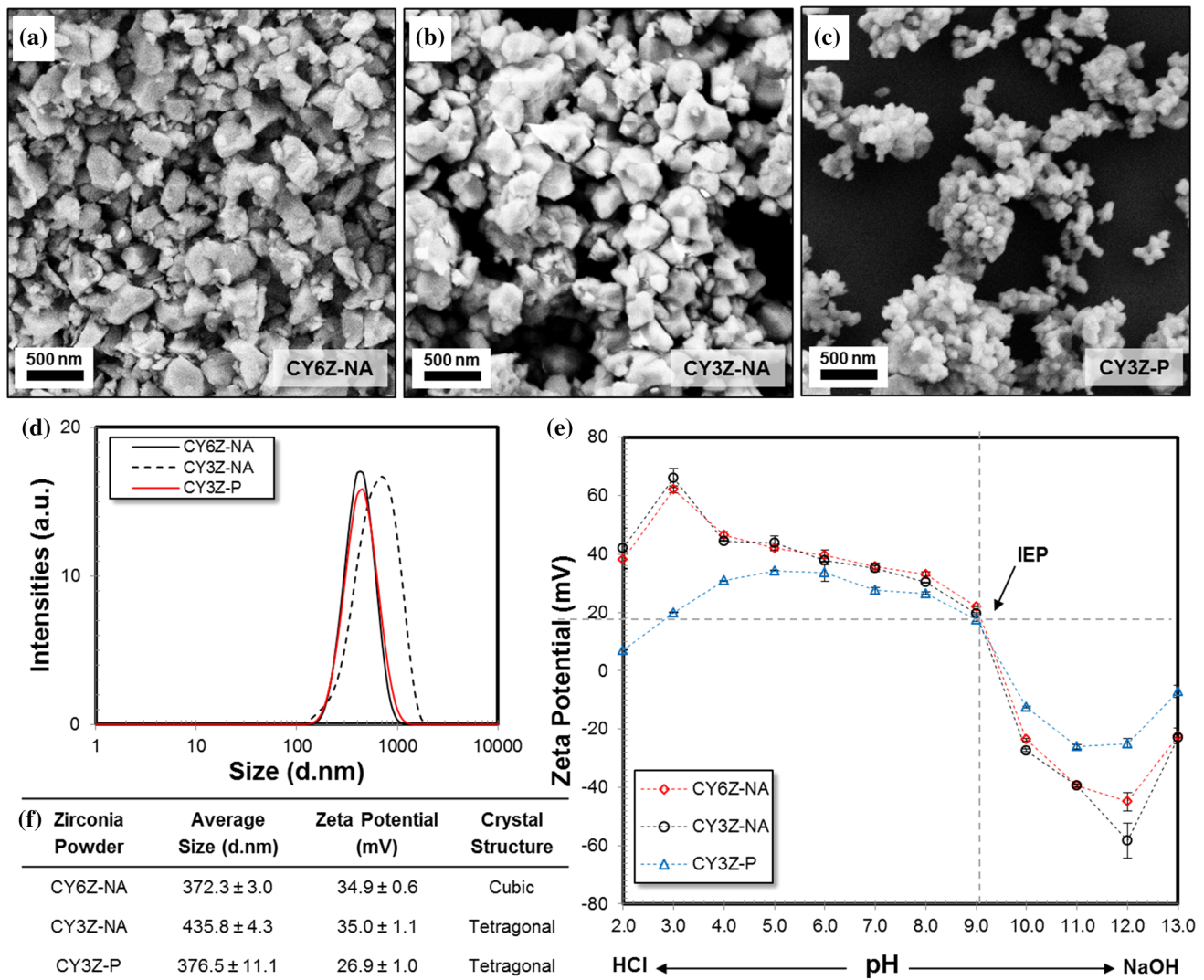


**Figure 1** SEM images of the commercial YSZ powders: **a** CY6Z-NA, **b** CY3Z-NA and **c** CY3Z-P. Plot of YSZ powders: **d** hydrodynamic size distributions in water at 25 °C and **e** zeta

potential at different pH conditions (pH 2.0–13.0) at 25 °C. **f** Tabulated YSZ powders properties at neutral condition.

water was consistent with the SEM observations, at  $372.3 \pm 3.0$ ,  $435.8 \pm 4.3$  and  $376.5 \pm 11.1$  nm, respectively. In addition to this, zeta potential analysis was also conducted for these YSZ powders at various pH conditions. From the zeta potential plot against the pH in Fig. 1e, the isoelectric point (IEP) of these YSZ powders lied in-between pH 9–10, above which the YSZ surface will be negatively charged. Therefore, when these YSZ powders were dispersed in water at neutral pH, the YSZ powders were expected to possess net positive surface charges (see table in Fig. 1f). From the XRD analysis (see ESI Figure S3), CY6Z-NA comprised of pure cubic phase, indicating the presence of fully stabilized zirconia

structure. Meanwhile, both CY3Z-NA and CY3Z-P comprised of tetragonal phase with slight trace of monoclinic phase, indicating the presence of partially stabilized zirconia structure.

**Ceramic suspensions formulation and rheological behaviours**

### Ceramic suspensions formulation and rheological behaviours

Following the traditional ceramic processing routes (e.g., tape casting or injection moulding), the YSZ ceramic powders were firstly fabricated into homogeneous ceramic suspensions with suitable rheological behaviour for the robocasting process [41, 42]. The previous zeta potential analysis (in Fig. 1e) suggested

these YSZ powders' surface charges in suspension were strongly dependent on their dispersing environment. When dispersed in water at neutral pH, the YSZ powder surfaces were dominated by positive charges with higher net positive charges in CY6Z-NA and CY3Z-NA than in CY3Z-P powders. After few minutes of sonication to break up agglomeration, it was observed that YSZ powders started to agglomerate severely again. Therefore, in order to promote better dispersion of YSZ powders in water, small anionic molecules that possessed carboxylic acid (–COOH) or hydroxyl (–OH) functional groups such as citric acid (denoted as CA;  $pK_a = 3.13$ ) and ascorbic acid (denoted as AA;  $pK_a = 4.2$ ) were employed as dispersant. Both citric acid and ascorbic acid have been previously reported in literature as suitable dispersant during alumina- and zirconia-based materials processing [43, 44]. Above its respective  $pK_a$ , the hydroxyl or carboxylic acid functional groups of these small molecules will be deprotonated, releasing  $H^+$  ions and resulting in negatively charged molecules. At pH between the dispersant  $pK_a$  and ceramics particles IEP, both negatively charged AA and CA dispersants have tendency to attach to the positively charged YSZ surface. In a simple demonstration, when dilute CY3Z-NA ( $1 \text{ mg mL}^{-1}$ ) was incubated with CA ( $1.25 \text{ mg mL}^{-1}$ ) in water at 1:10 CA/CY3Z-NA mass ratio, the CY3Z-NA zeta potential shifted from  $35.0 \pm 1.1$  to  $-24.7 \pm 1.2$  mV. The shift indicated the adsorption of the negatively charged molecules onto the positive CY3Z-NA surface. The addition of CA dispersant also caused the average CY3Z-NA hydrodynamic size to decrease slightly from  $435.8 \pm 4.3$  to  $324.4 \pm 6.5$  nm, indicating that the negatively charged dispersant adsorbed on the YSZ surface helped to de-flocculate YSZ powders by providing sufficient electrostatic repulsions. Generally, in order to promote strong adsorption of the dissociated AA or CA onto YSZ powders, the YSZ surface must possess sufficient positive binding sites while the AA or CA must be significantly dissociated. Thus, intermediate pH between the dispersant  $pK_a$  and the ceramic IEP (i.e., pH around 3.0–6.0) was the most suitable condition to process the CY6Z-NA, CY3Z-NA and CY3Z-P powders into the ceramic suspensions. Based on this analysis, anionic CA and AA dispersant as well as anionic binder system (PVA) were selected as dispersant–binder systems during the formulation ceramic suspensions for

robocasting process. The printable CY6Z-NA, CY3Z-NA and CY3Z-P ceramic suspensions were prepared by firstly homogenizing the dispersant solution (in water) with the YSZ ceramic powders, followed by the addition of PVA binder and PEG plasticizer. The mixture was then further homogenized and aged to allow excess water evaporation to obtain homogeneous ceramic suspensions with suitable rheology for robocasting.

In robocasting, the concentrated ceramic suspension was deposited onto print substrate through a small orifice. During this process, the suspension will be subjected to significant shear stress (please refer to ESI Section S4 for detailed explanation). Thus, the concentrated ceramic suspension's rheological behaviour is critical in ensuring the paste printability. A simple study was conducted to understand the influence of dispersant and powder solid loading on the resultant ceramic paste viscosity and printability. In this study, CY3Z-P powders with higher specific surface area than CY6Z-NA or CY3Z-NA was selected. Figure 2a summarizes the viscosities at both zero and high shear rate of CY3Z-P suspensions fabricated using different AA dispersant to CY3Z-P mass ratio (from 0 to 1.66 wt%). The as-obtained CY3Z-P suspensions were loaded into plastic syringe equipped with  $410\text{-}\mu\text{m}$  nozzle, extruded into a mould, dried and sintered at  $1500\text{ }^\circ\text{C}$  for 10 h (see the SEM images summary in Figure S5). Without dispersant (at 0 wt%), the paste viscosity was too high ( $>4000 \text{ Pa s}$ ) and the sintered CY3Z-P surface was too rough due to the inadequate particles de-flocculation during paste formulation, indicating thick and inhomogeneous paste. When the dispersant amount was increased gradually, the resultant paste viscosity decreased significantly while the sintered CY3Z-P surface roughness decreased. Homogeneous CY3Z-P suspension was obtained with dispersant amount as low as 0.21 wt% AA (Figure S5c). At 0.41 wt% AA dispersant, the sintered CY3Z-P surface roughness slightly increased which indicated the aggregation of CY3Z-P particles in the suspension. Such aggregation can be ascribed to the presence of excess dispersant that caused depletion flocculation [45]. For CY3Z-P powders, approximately 0.2–0.3 wt% of AA dispersant was enough to provide sufficient electrostatic and steric stabilization that significantly reduced the inter-particle interactions, preventing the YSZ ceramic particles to flocculate or to form long-range rigid network. This resulted in ceramic suspensions with minimum viscosity.

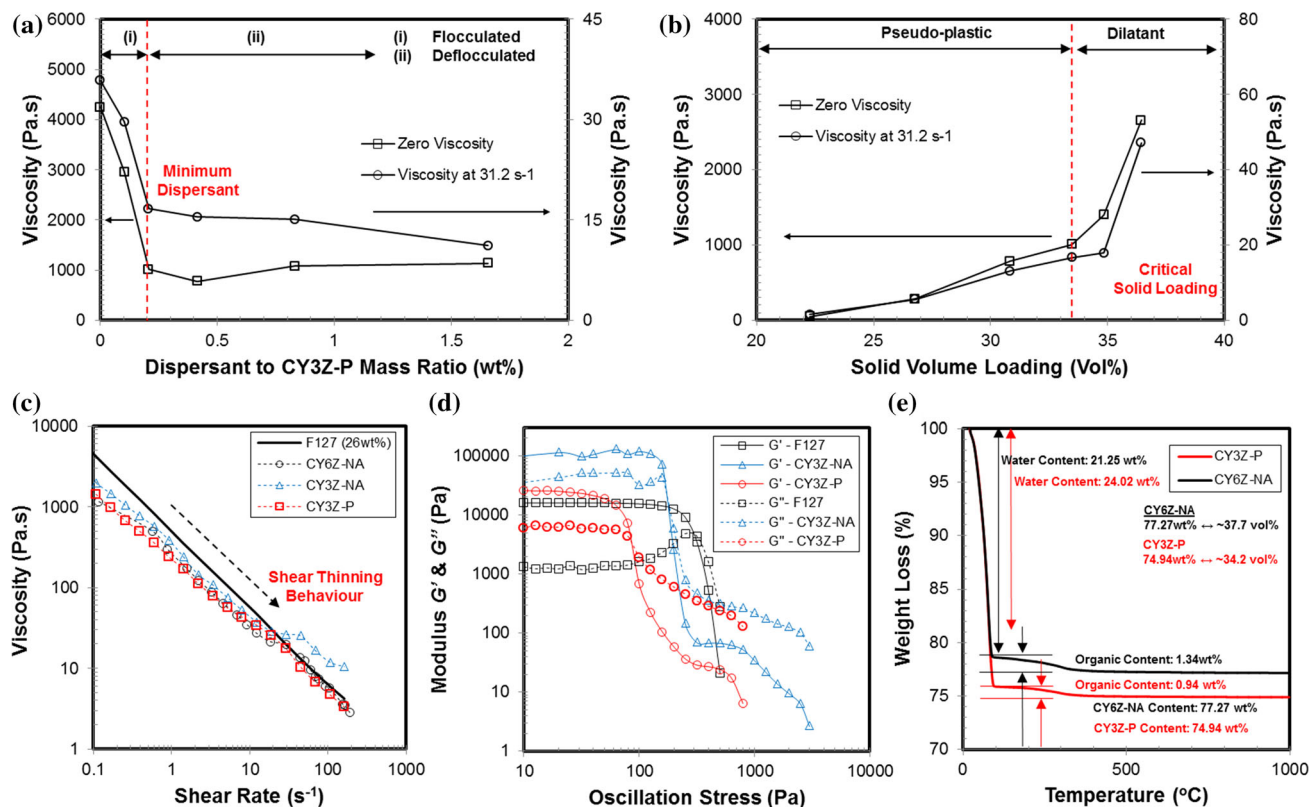


**Figure 2** Rheological properties of aqueous YSZ suspensions. Viscosity of CY3Z-P suspension against: **a** the dispersant/CY3Z-P mass ratio and **b** the solid loading (dispersant/CY3Z-P ratio: 0.41 wt% dwb). The solid volume loadings (22.3–36.5 vol%) refer to the initial solid loading before mixing and water evaporation (i.e., volume of CY3Z-P powders added against the total volume). **c** Log–log plot of CY6Z-NA, CY3Z-NA and CY3Z-P paste

viscosities as a function of the shear rate (flow ramps from 0 to 200 s<sup>-1</sup>). **d** DMA log–log plot of shear modulus as a function of shear stress for CY3Z-NA and CY3Z-P pastes (oscillation stress from 0.1 up to 2000 Pa). The flow ramp and DMA of pure F127 hydrogels suitable for robocasting with 26 wt% loading were included for comparison. **e** Thermogravimetric analysis of the aqueous CY6Z-NA and CY3Z-P robocasting paste.

At the optimum AA dispersant amount (0.21 wt%), the solid content of CY3Z-P was varied from 22.2 to 36.5 vol% while retaining the dispersant/CY3Z-P mass ratio. Herein, the solid volume loadings refer to the volume of CY3Z-P powders added with respect to the total volume of the paste. Figure 2b summarizes the CY3Z-P suspensions rheological behaviour against the solid loading content. The overall viscosities at zero and high shear rate were found to increase with the solid loadings of CY3Z-P. From the results, two-distinct slurry behaviour regions were observed. At low solid content (22.3 vol%), the well-dispersed suspensions already exhibited non-newtonian rheological behaviour with relatively low viscosity. At slightly higher solid loading content (26.8, 30.8 and 33.5 vol%), viscosities increased significantly due to strong YSZ inter-particle interactions and collisions. Within this range, the ceramic suspensions

started to exhibit strong pseudo-plastic rheological behaviour. In addition to this, the CY3Z-P suspensions exhibited notable shear-thinning properties and ceased to flow at zero shear rate. At higher solid loading (34.9 and 36.5 vol%), the CY3Z-P particles within the suspensions became strongly restricted and therefore suspensions with significantly high viscosity were obtained. Beyond 36.5 vol% solid content, the resultant CY3Z-P suspensions ceased to flow even at higher shear rate, resulting in dilatant mass and causing poor printability. From the rheology analysis, the CY3Z-P suspensions between 30.8 and 34.9 vol% solid loadings possess good printability during robocasting. From the SEM analysis of the sintered CY3Z-P samples (Figure S6), samples with low solid loading content (22.3, 26.8 and 30.8 vol%) have low green densities and therefore resulted in poor sinterability, as indicated by the



presence of pores after sintering (Figure S6a, b). The porosity was due to the large amount of solvent evaporation during the drying step which disrupted the densification during the sintering process. Despite such low loading, no drying crack was observed from sintered CY3Z-P samples due to the use of releasing agent on the mould, which promoted controlled shrinkage. At high-solid loading content (34.9 and 36.5 vol%), pores presence was also there in the sintered CY3Z-P samples due to the high-viscosity-induced air bubbles trapping during the CY3Z-P suspensions fabrication. Overall, homogeneous CY3Z-P suspension was obtained with the optimum solid loading content of 33.5 vol%. For robocasting process, it is critical to work with the ceramic suspension with solid loading that was relatively close to the pseudo-plastic to dilatant transition whereby the suspension exhibited highly shear thinning behaviour [20]. Based on Fig. 2b, the critical solid loading for CY3Z-P powders with 0.2 wt% AA dispersant was 33.5 vol%. From our unpublished results, the pseudo-plastic to dilatant transition occurs at approximately 36.5 vol% for both CY6Z-NA and CY3Z-NA ceramic suspensions with approximately 0.32 wt% CA dispersant. An attempt to disperse CY3Z-P using CA dispersant resulted in severe particles flocculation which increased the viscosity significantly. On the other hand, an attempt to disperse CY6Z-NA/CY3Z-NA using AA dispersant resulted in printable paste at slightly lower solid volume loading as compared to CA dispersant. Since (1) CA has lower pKa than AA and (2) CY3Z-P has lower surface charges than CY6Z-NA/CY3Z-NA powder, such behaviour can be presumably ascribed to the pH difference in the final YSZ suspensions as well as the different amount surface charges stabilization required for CY3Z-P as compared to CY6Z-NA/CY3Z-NA powder.

For the robocasting process, three different YSZ suspensions were fabricated with CY6Z-NA, CY3Z-NA and CY3Z-P powders. The apparent viscosity of these printable YSZ suspensions at increasing shear rates (0.01–200 s<sup>-1</sup>) is plotted in Fig. 2c. Despite the different formulations of each respective suspension, these YSZ suspensions showed similar flow behaviour with extensive shear thinning characteristic behaviour even at low shear rate (<10 s<sup>-1</sup>), indicated by the exponential viscosity decrease with the increase in shear rate. Based on the estimated shear rates calculated from the printer and nozzle

configurations (see Figure S4) using Hagen–Poiseuille equation, shear rate over 30 s<sup>-1</sup> (up to 200 s<sup>-1</sup>) at the wall of the nozzle was expected during robocasting process. From Fig. 2c, at shear rate above 10 s<sup>-1</sup>, the YSZ suspensions were found to reach the typical robocasting viscosity requirement of 10–100 Pa s<sup>21</sup>. Based on these result, increasing the printing speed which inherently increasing shear rate during robocasting was possible; however, it has to be performed carefully as fast print speed will increase the risk of having inaccurate print head path especially during a 90° turn, causing sharp corners to become round corners. For dense or solid sample, three different parameters namely (1) the internal filling rastering pattern, (2) the spacing between adjacent filaments and (3) the material feeding rate have to be adjusted in order for the deposited extrudate to fuse completely with the adjacent filaments during the printing as well as with the filaments underneath in the z-direction, minimizing the amount of possible defect or cavity that may develop. Any trapped air bubbles or cavity will leave pores or defects after debinding and sintering processes. When the extrudate is deposited too close to the adjacent one, overfilling may occur which significantly causes the materials to build up in the nozzle and dragged along the printing process, inadvertently causing unnecessary shearing and movement to the adjacent and underneath filaments. Therefore, from our trials and errors, for printing YSZ solid samples, the spacing between the extrudates (i.e. line width over height ratio) was fixed at approximately ~1.45 times of the nozzle size while the material feeding rate was increased slightly than required to ensure over-extrusion of the paste that squeeze the filament together during printing. Such line spacing setting is less stringent during the printing of YSZ porous samples (e.g. mesh). For porous samples, the line width over height ratio was usually set to ~1 to ~1.2 times as a slight over-extrusion is still needed in order to ensure that the currently deposited layer will adhere to the underneath layer.

Besides the flow ramp, the viscoelastic behaviour of the CY3Z-P and CY3Z-NA pastes used in the robocasting process was studied by dynamic mechanical analysis (DMA). The paste storage modulus ( $G'$ ) and loss modulus ( $G''$ ) variation with increasing shear stress is summarized in Fig. 2d. For comparison, non-colloidal gel comprised of 26 wt% pluronic F127 in water was also measured at similar

condition and setting. The 26 wt% F127 gel was found to be suitable for robocasting process. In demonstration (see ESI Figure S7), several structures such as hollow cylindrical cup, cube and mesh structures have been printed successfully using the F127 gel.

From Fig. 2d, both CY3Z-NA and CY3Z-P pastes exhibited a linear viscoelastic response at low shear stress. As the shear stress oscillation amplitude increased, the storage modulus ( $G'$ ) decreased and the loss modulus ( $G''$ ) rises. The yield stresses ( $\tau_y$ ) were determined at which the  $G'$  is equal to the  $G''$ . Higher storage modulus for CY3Z-NA and CY3Z-P paste as compared to 26 wt% F127 gel can be attributed to the formation of stiff network due to YSZ particles and dispersant/binder interactions. From Fig. 2d, the yield stress of CY3Z-P, CY3Z-NA and 26 wt% F127 paste was found to be 100.1 Pa, 158.5 Pa and 316.3 Pa, respectively, while the equivalent storage modulus or stiffness of CY3Z-P, CY3Z-NA and 26 wt% F127 paste was found to be 24.7, 111.0 and 16.1 kPa, respectively. On the other hand, both  $K$  and  $n$  were determined from the fitting of  $\log(\tau - \tau_y) = \log(K) + n \cdot \log(\dot{\gamma})$ . From the fitting, the viscosity parameter  $K$  were found to be 107.7, 182.7 and 144.8 Pa s, respectively, while the flow behaviour index  $n$  were found to be 0.35, 0.43 and 0.12, respectively. These values are summarized in Table 1. Both CY3Z-NA and CY3Z-P pastes and 26 wt% F127 gel exhibited yield stress ( $\tau_y > 0$ ) with extensive shear thinning behaviour above the yield stress ( $n < 1$ ) which are required for robocasting process. A yield stress ( $>0$ ) is required to allow the robocast materials to maintain the shape fidelity after being extruded out of the nozzle (and after removal of shear stress) and to allow the extruded layers to withstand the weight of the subsequently deposited layers above. Yield stress of 26 wt% F127 is large enough ( $\tau_y > 200$  Pa) to allow tall structures to be printed out successfully. However, because of its relatively large yield stress, 26 wt% F127 has to be

extruded at  $\geq 1.3\times$  of materials feed rate (i.e, higher pressure) as compared to CY3Z-NA and CY3Z-P pastes using 410- $\mu\text{m}$  nozzle diameter. CY3Z-P paste that has the lowest yield stress of 100.1 Pa among the formulated paste may not be able to withstand its own weight after printing. In order to assess the printability of CY3Z-P paste, a simple study was conducted. The viscosity and the shear stress of CY3Z-P paste with decreasing shear rate (denoted as falling curve; from 200 to 0  $\text{s}^{-1}$ ) was recorded after increasing the shear rate (rising curve) from 0 to 200  $\text{s}^{-1}$ . The log–log plot of viscosity and shear rate against the decreasing shear rate are given in Figure S8a and Figure S8b, respectively. From Figure S8a, the initial zero shear rate viscosity was 9.06 kPa s ( $\tau = 113.8$  Pa). When the shear rate reverted back to 0  $\text{s}^{-1}$ , the viscosity of CY3Z-P returned close to its original zero shear rate viscosity at 8.17 kPa s ( $\tau = 101.6$  Pa). Such similar behaviour was observed from 26 wt% F127. The initial zero shear rate viscosity was 34.45 kPa s ( $\tau = 402.9$  Pa). When the shear rate reverted back to 0  $\text{s}^{-1}$ , the viscosity of 26 wt% F127 returned viscosity at 25.35 kPa s ( $\tau = 316.4$  Pa). From the rheological analysis, CY3Z-P shear thinning behaviour should be reversible and the extruded structure will gain back its original viscous state once the shear stress is removed. Its low yield stress also allows the paste to be printed at much lower pressure, which is beneficial for low-cost 3D printer (using 3Dison Multi). In order to verify this behaviour, CY3Z-P paste was robocast into large and tall structure. Figure S8c, d shows the snapshot of the robocasting process using CY3Z-P paste during the fabrication of a wide hollow box and a tall hollow box at printing speed of 5 mm/s. During the printing, no materials buildup was observed in the nozzle tip. On top of this, during the printing and after printing, the printed structures were stable without warping and collapsing despite its low yield stress (see Video S1, S2 and S3 for more details). This indicated that CY3Z-P was printable, and the extruded structure was able to withstand its own weight.

In the previous rheological study (Fig. 2b), the solid loadings of CY6Z-NA, CY3Z-NA and CY3Z-P paste were determined by calculating the YSZ powder loading against the total volume of the paste (powder with solvent). In order to determine the final consolidated solvent, organic additives and YSZ powders contents in the printable suspensions,

**Table 1** Rheological properties of CY3Z-NA, CY3Z-P as well as 26 wt% F127 robocasting paste

Sample	$G'_{\text{eq}}$ (kPa)	$\tau_y$ (Pa)	$K$ (Pa s)	$N$
CY3Z-P	24.7	100.1	107.7	0.35
CY3Z-NA	111.0	158.5	182.7	0.43
F127 (26 wt%)	16.1	316.3	144.8	0.12

thermogravimetric analysis (TGA) was conducted for CY6Z-NA and CY3Z-P suspensions prepared for the robocasting process. The temperature-dependent weight loss curve of both suspensions (Fig. 2d, e) indicated three different weight loss regions. Between room temperature to 150 °C, approximately 21.25 and 24.02 wt% weight loss in CY6Z-NA and CY3Z-P suspensions corresponded to the water evaporation. The subsequent weight loss of about 1.34 and 0.94 wt% during heating from 150 to 450 °C can be ascribed to the burnout of various organic additives content in CY6Z-NA and CY3Z-P suspensions, respectively. Finally, when the samples were heated to temperature above 500 °C, the weight loss curve reached a plateau, indicating constant residual sample weight. This remaining weight corresponded to the 77.27 wt% of CY6Z-NA and 74.94 wt% of CY3Z-P content in the suspension. These values were equivalent to 37.7 vol% of CY6Z-NA and 34.2 vol% of CY3Z-P solid loading. As the YSZ contents in CY6Z-NA and CY3Z-P during the initial paste formulation process were 36.5 and 33.5 vol%, respectively, the discrepancy indicated significant water evaporation during the process. The overall organic additives content were found to be less than 2 wt% as compared to the CY6Z-NA and CY3Z-P dry weight. It was also revealed that CY6Z-NA powder required slightly higher organic additives content as compared to CY3Z-P powders. In most cases, organic additives concentrations have to be as low as possible to ensure complete binder burnout process. The TGA results suggested that an intermediate debinding temperature as low as 500–600 °C should be sufficient for a complete binder burnout. To study the sintering conditions, the as-prepared YSZ suspension containing CY6Z-NA, CY3Z-NA or CY3Z-P powders was robocast into a standard cube shape (10 mm width) using 410- $\mu\text{m}$  tapered plastic nozzle. The green body was printed directly on top of acrylic substrate in an ambient condition. Linear shrinkage by 8–10% of the original dimension was observed during the drying process. No warping or drying cracking was observed during the forming and drying process due to the aforementioned controlled shrinkage strategy. After drying at ambient condition, the YSZ green body with cube shape weight was around 2.0–2.2 grams (approximately 33–36% of the YSZ theoretical density). Therefore, the YSZ green body density has further densified to more than 45% of YSZ theoretical density after

drying. These samples were then sintered under pressure-less and atmospheric conditions at various conditions ( $\geq 1400$  °C for 5, 10 or 20 h). During the sintering process, slow ramping up process at  $1$  °C  $\text{min}^{-1}$  was preferred to prevent samples cracking and deformation while an intermediate temperature of 600 °C for 1 h was opted for the debinding process.

### Fabrication of fully stabilized zirconia structures: CY6Z-NA

To obtain fully stabilized zirconia samples, cubic CY6Z-NA powder (6 mol % yttria content and 0.25 wt%  $\text{Al}_2\text{O}_3$ ) was employed as starting precursor. For commercial powders, small trace of  $\text{Al}_2\text{O}_3$  was usually added as a sintering aid agent [46, 47]. To study the influence on sintering temperature towards the microstructure of CY6Z-NA, the robocasted CY6Z-NA cubic-shape green bodies were sintered at 1450, 1500, 1550, 1600 and 1700 °C for 20 h (Fig. 3a). After sintering, the cubic-shape geometry was retained. The microstructure analysis of the sintered CY6Z-NA surfaces (given in Fig. 3b–f) revealed homogeneous grains packing with the absence of any open pores structure. As the CY6Z-NA green body was sintered under pressure-less and normal atmospheric conditions, the absence of any pores on the sintered surface indicated the successful densification process. Moreover, it was observed that the YSZ grain size increases with increasing sintering temperature. In order to estimate the sintered parts grain size, the individual grain area (from SEM image) was measured using ImageJ. By assuming circular shape for each grain, the corresponding average grain diameters were calculated. The average grain sizes of the CY6Z-NA parts were  $1.40 \pm 0.53$ ,  $1.96 \pm 0.72$ ,  $2.85 \pm 1.44$ ,  $4.13 \pm 1.51$  and  $6.75 \pm 2.04$   $\mu\text{m}$  when sintered for 20 h at 1450, 1500, 1550, 1600 and 1700 °C, respectively. Besides the increase in average grain size, the grain size distribution also significantly broadened with the increase in sintering temperature (Fig. 3g). This indicated a significant grain growth at higher temperature. After sintering, the cubes showed additional 15–20% linear shrinkage from the green body dimension (approximately 25–30% shrinkage from the CAD model). Higher shrinkage was registered in the  $z$ -direction than in the lateral  $x$ -direction and  $y$ -direction, indicating an anisotropic shrinkage during sintering. The SEM images



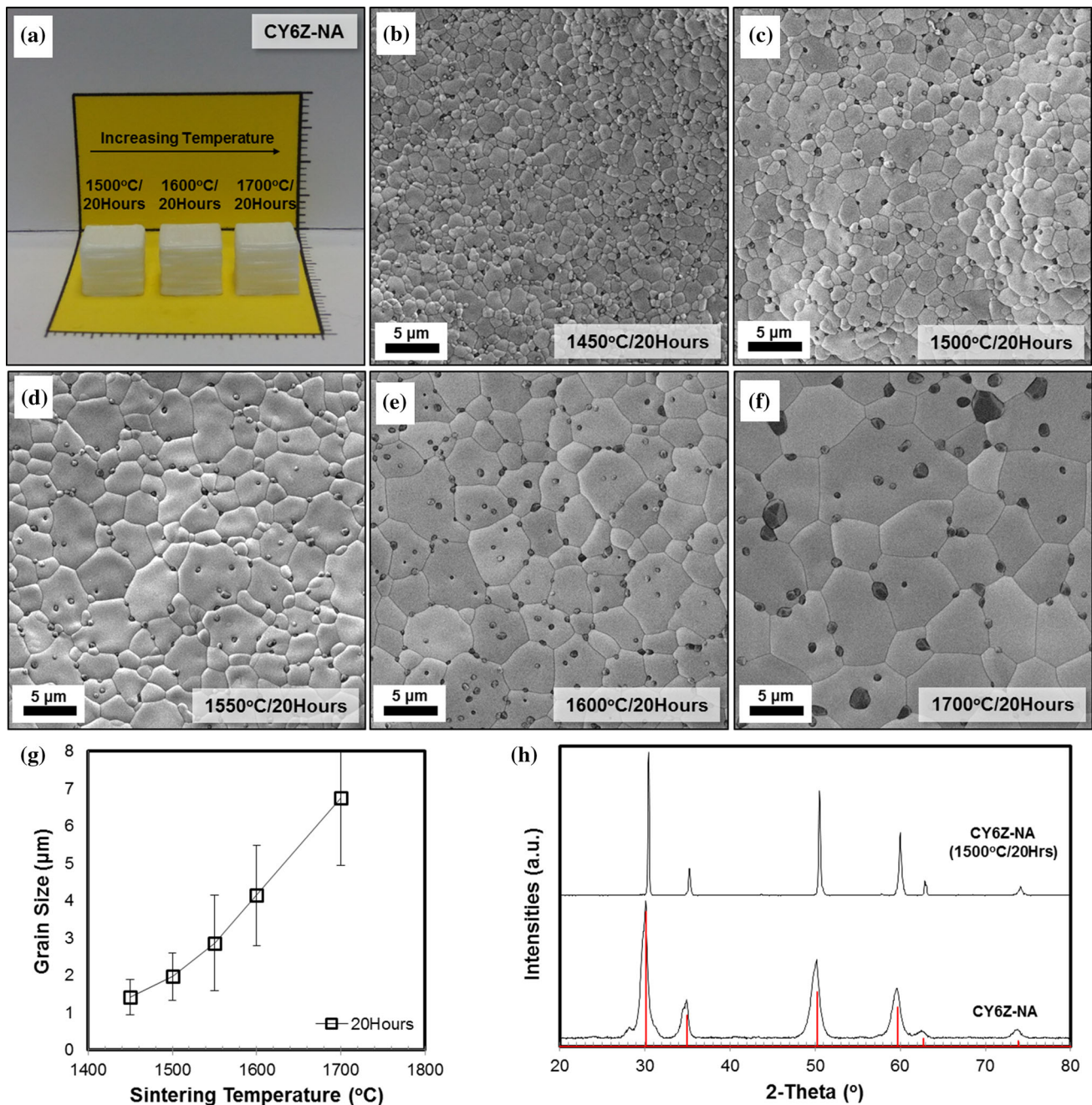


**Figure 3** a CY6Z-NA samples sintered at different conditions. SEM images of samples sintered at b 1450 °C, c 1500 °C, d 1550 °C, e 1600 °C and f 1700 °C for 20-h duration. g Plot of

the sintered CY6Z-NA parts revealed the presence of the second-phase particles or inclusions (darker contrast). EDX elemental mapping was performed on one of the sintered CY6Z-NA samples at 1500 °C/20 h (see ESI Figure S9). From the mapping, the darker particles in both YSZ grain interior and grain boundary corresponded to the Al element which

the CY6Z-NA grain sizes against the sintering temperature. h XRD patterns of CY6Z-NA powders and sintered sample (1500 °C/20 h).

indicated the presence of  $\text{Al}_2\text{O}_3$  particles or inclusions. The EDX elemental analysis on CY6Z-NA powder precursor revealed the presence of approximately 4.2 wt% of alumina. After sintering, the EDX elemental analysis revealed the presence of 5.63 wt% alumina in the surface of the sintered CY6Z-NA (1500 °C/20 h).



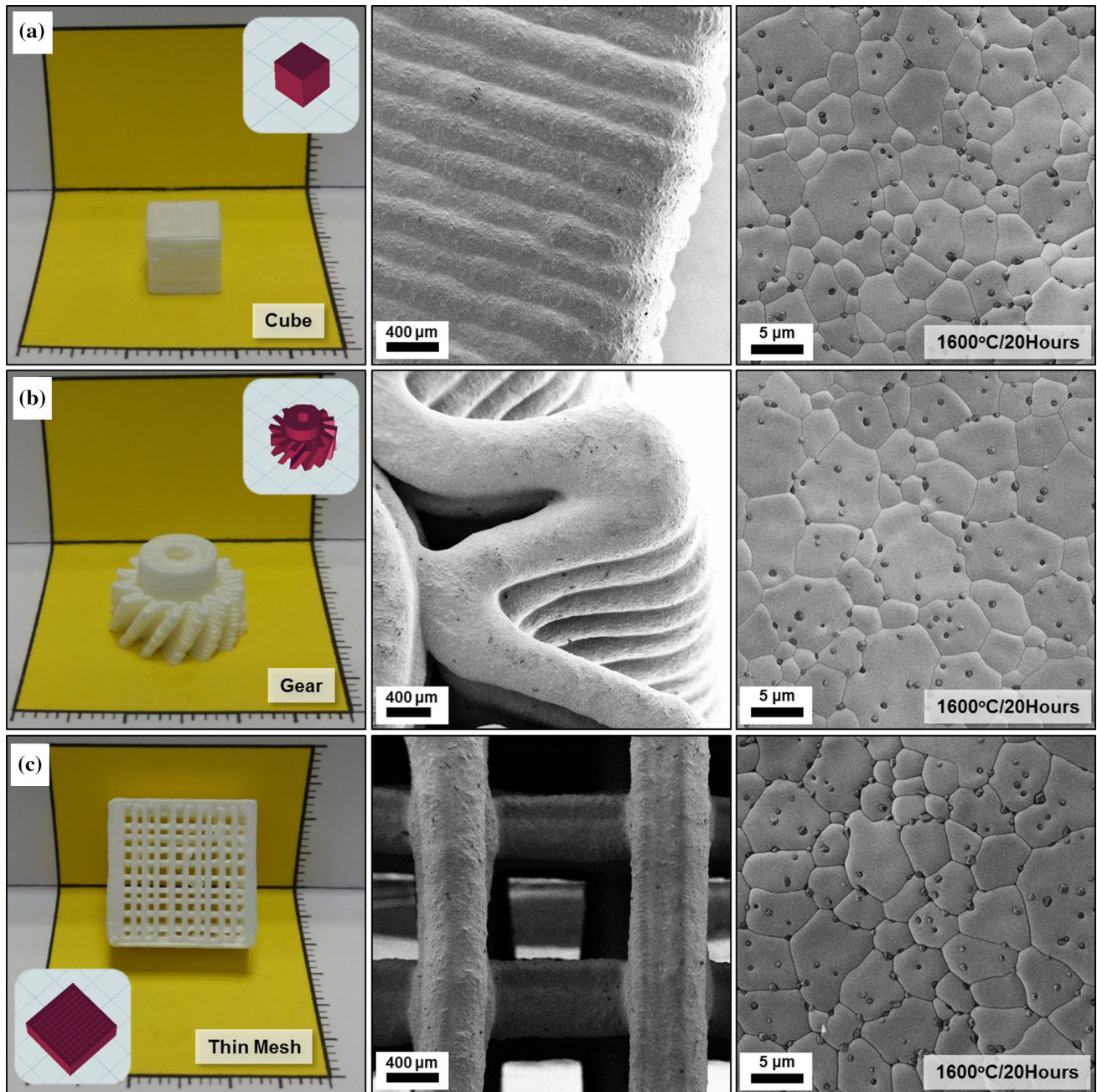
The crystalline phases of the sintered CY6Z-NA samples were analysed by XRD. As shown in Fig. 3h, the diffraction peaks in the sintered CY6Z-NA sample (1500 °C/20 h) XRD pattern were indexed against the standard reflection pattern of cubic zirconia ( $c\text{-ZrO}_2$ ; JCPDS 27-0997) at  $2\theta = 30.3^\circ$ ,  $35.0^\circ$ ,  $50.3^\circ$  and  $59.8^\circ$ . These peaks corresponded to  $c\text{-ZrO}_2$  (111), (200), (220) and (311) planes, respectively. No additional impurity phase was present in the XRD pattern, suggesting the complete formation of highly crystalline fully stabilized YSZ structure. Additional XRD results for CY6Z-NA sintered at different temperatures are given in Figure S10. Even at 1700 °C,  $c\text{-ZrO}_2$  phase was still retained without any formation of monoclinic zirconia ( $m\text{-ZrO}_2$ ). Further analysis of sintered CY6Z-NA sample was also conducted by XPS (see Figure S11). The survey scan spectrum of both CY6Z-NA powder and sintered bulk structure (Figure S11a) indicated the presence of 5 elemental compositions on the surface of the samples: C 1s, Zr 3d, Y 3d, O 1s and Al 2p. The C 1s peak (284.6 eV) was used as reference for the binding energy correction. No other impurity elements were detected in the sample within the detection limit. The corresponding high-resolution scan spectra of respective elements are summarized in Figure S11b–e. The C 1s spectrum of both CY6Z-NA powders and sintered sample was fitted and assigned into their corresponding carbon atoms components at different positions. The presence of C=C peak at 284.6 eV in Figure S11b on both CY6Z-NA powders and sintered sample was due to the inevitable overlaying hydrocarbon layer contamination during measurement. Two additional peaks at 286.0 eV and 288.2 eV in CY6Z-NA powder can be ascribed to the presence of C–O and C=O bonds from residual organic content of the commercial powder. These C–O and C=O bonds peak diminished in sintered CY6Z-NA, indicating a clean binder burnout during the debinding process. Figure S11c and Figure S11d summarize the Zr 3d and Y 3d spectra obtained from CY6Z-NA powder and sintered CY6Z-NA sample. Similar Zr  $3d_{5/2}$  and Zr  $3d_{3/2}$  peaks at 181.7 eV and 184.2 eV with spin-orbit splitting of 2.5 eV as well as Y  $3d_{5/2}$  and Y  $3d_{3/2}$  peaks at 156.8 eV and 158.8 eV with spin-orbit splitting of 2.0 eV were observed for both CY6Z-NA powder and sintered CY6Z-NA samples. This indicated that the chemical state in the cubic structure of original YSZ powder did not change, even after high-temperature sintering. The O 1s spectrum in

Figure S11e indicates the presence of the main peak at 529.6 eV which corresponded to the lattice oxygen of YSZ structure and the shoulder peak at above 531.1 eV which corresponded to the OH bond. For the sintered CY6Z-NA samples, the Al 2p peak at 74.2 eV (Figure S11f) suggested the presence of sintering aid  $\text{Al}_2\text{O}_3$ .

To demonstrate the versatility of robocasting method in fabricating dense fully stabilized YSZ structures, several green bodies with unique morphology were printed and sintered. These were inclusive of cube, coin, gear, cylinder, ring, hexagon mesh and rectangular mesh structures (several sintered parts were included in ESI Figure S12), highlighting the high degree of freedom of such solid free-forming fabrication. Selected CY6Z-NA samples with different morphology were analysed. First of all, a simple cube CY6Z-NA structure side view was examined by SEM (Fig. 4a). The observed filaments stacking in the z-direction demonstrated that the adjacently deposited layers fused cleanly after sintering to form a solid dense structure, leaving no cavity or residual pores. On top of this, no overflowing of ceramic paste was observed. Similarly, the sintered CY6Z-NA helical gear was also successfully sintered without any warping after densification process. The SEM image of the printed gear tooth (Fig. 4b) suggested that the extrudates were stacked uniformly in the z-direction with a slight overhanging to form the helical blade structure. For a more complex morphology, rectangular mesh with cross-hatched structure was designed and printed. The SEM image of this mesh in Fig. 4c indicated the alternating layers between the deposited struts (at 500  $\mu\text{m}$  diameter) were still preserved after sintering process. The comparison between the SEM images given in Figs. 3e and 4 suggested that similar grain size and grain size distributions can be obtained regardless of the sample morphologies, when samples were sintered at similar condition (e.g., 1600 °C/20 h).

### Fabrication of partially stabilized zirconia structures: CY3Z-NA

To obtain partially stabilized zirconia samples, CY3Z-NA powder with predominantly tetragonal phase (3 mol % yttria content and 0.25 wt%  $\text{Al}_2\text{O}_3$ ) was employed as starting precursor. To study the influence on sintering temperature towards the



**Figure 4** Sintered CY6Z-NA structures: **a** cube, **b** helical gear and **c** rectangular thin mesh structures. From left to right photographs, low- and high-magnification SEM images (*inset* CAD model of respective sample).

microstructure of CY3Z-NA, the robocasted CY3Z-NA cubic-shape green bodies were sintered at different conditions: (1) 1400 °C for 10 h, (2) 1450 °C for 5, 10 and 20 h as well as (3) 1500 °C for 10 and 20 h. The microstructures analysis of the sintered CY3Z-NA surfaces (given in Fig. 5a–f) revealed homogeneous and densely packed submicron-size grains. From the microstructure analysis, the average CY3Z-NA grain size when sintered at 1450 °C was

$0.59 \pm 0.18$  (Fig. 5a),  $0.70 \pm 0.23$  (Fig. 5b) and  $0.92 \pm 0.28$  (Fig. 5c) when sintered at 5, 10 and 20 h, respectively. When the sintering temperature was reduced to 1400 °C for 10 h, the average CY3Z-NA grain size at  $0.55 \pm 0.18$  μm was comparable with the grain size of CY3Z-NA sample sintered at 1450 °C for same duration. However, from Fig. 5d, numerous open pores were observed on the surface of the sintered CY3Z-NA at 1400 °C for 10 h. Thus, a



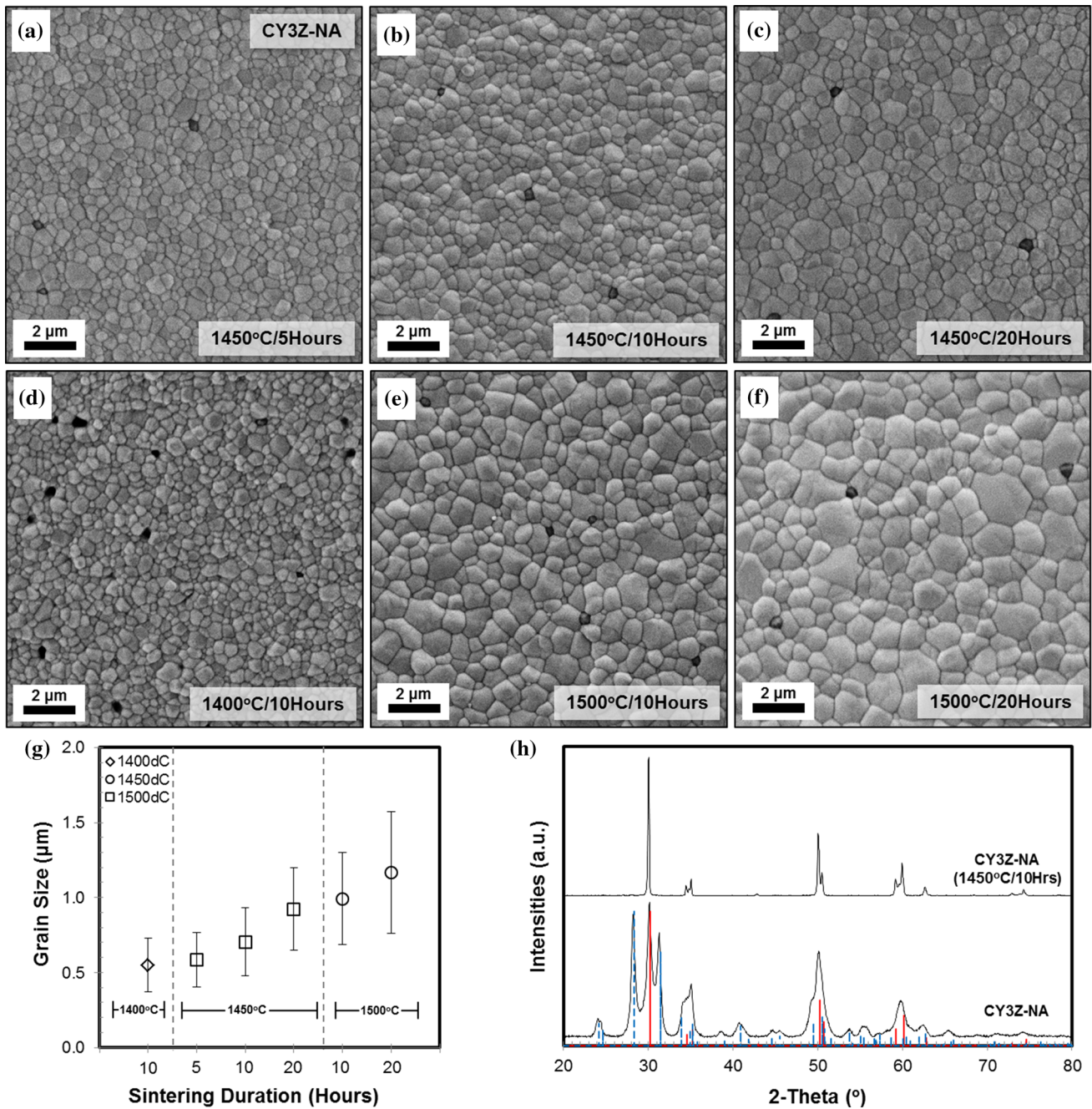


**Figure 5** SEM images of samples sintered at **a** 1450 °C/5 h, **b** 1450 °C/10 h, **c** 1450 °C/20 h, **d** 1400 °C/10 h **e** 1500 °C/10 h, **f** 1500 °C/20 h. **g** Plot of the CY3Z-NA grain sizes against the

sintering condition. **h** XRD patterns of CY3Z-NA powders and sintered sample (1450 °C/10 h).

minimum temperature of 1450 °C was required to successfully sinter the CY3Z-NA green bodies under pressure-less sintering (normal atmospheric conditions) into dense structure. When sintered at higher temperature 1500 °C, further grain growth occurred and the average CY3Z-NA grain size increased to  $0.99 \pm 0.31$  and  $1.17 \pm 0.41$  μm when sintered at 10

and 20 h, respectively. Based on this comparison, the average CY3Z-NA grain size increased with the increase in both temperature and duration. In contrast to the CY6Z-NA samples, the increase in average CY3Z-NA grain size did not cause significant change in the grain size distribution (Fig. 5g). Similar to CY6Z-NA samples, linear shrinkage of

approximately 25–30% from the CAD model was also observed for CY3Z-NA samples. As the CY3Z-NA has similar  $\text{Al}_2\text{O}_3$  content as compared to the CY6Z-NA, the presence of the second-phase particles (darker contrast) can be similarly ascribed to the presence of  $\text{Al}_2\text{O}_3$  particles or inclusions.

With approximately 3 mol % yttria blends, tetragonal zirconia polycrystalline phase was expected from the sintered CY3Z-NA sample. The crystalline phases of the sintered samples were analysed by XRD. As shown in Fig. 5h, in all the present diffraction peaks in the sintered CY3Z-NA samples (1450 °C/10 h) XRD pattern was indexed against the standard reflection pattern of tetragonal zirconia ( $t\text{-ZrO}_2$ ; JCPDS 80-0965) at  $2\theta = 30.2^\circ$ ,  $34.6^\circ/35.3^\circ$ ,  $50.2^\circ/50.7^\circ$ ,  $59.3^\circ/60.2^\circ$ ,  $62.9^\circ$ . These peaks corresponded to  $t\text{-ZrO}_2$  (101), (002)/(110), (112)/(200), (103)/(211), (202) planes, respectively. The  $t\text{-ZrO}_2$  structure was clearly emphasized from the presence of diffraction peaks splitting at  $2\theta$  around  $35^\circ$ ,  $50^\circ$  and  $60^\circ$ . Whereas for  $c\text{-ZrO}_2$  structure, such diffraction planes were forbidden in cubic symmetry and only single diffraction peak was expected for the aforementioned Bragg's reflection. The minor  $m\text{-ZrO}_2$  impurity phase that existed in the CY3Z-NA powder precursor disappeared from the sintered CY3Z-NA XRD patterns (1450 °C/10 h). No additional impurity phase was present in the  $t\text{-ZrO}_2$  XRD pattern, suggesting the complete formation of tetragonal polycrystalline or partially stabilized YSZ structure. Additional XRD result for CY3Z-NA sintered at 1500 °C for 10 h is given in Figure S13. Even at slightly higher temperature of 1500 °C,  $t\text{-ZrO}_2$  phase was still retained without any formation of  $m\text{-ZrO}_2$  phase.

To demonstrate the versatility of robocasting method in fabricating dense partially stabilized YSZ structures, several green bodies with unique morphology were printed and sintered. These were inclusive of cube, cylinder, ring, monolith, hollow box and rectangular mesh structures (several sintered parts were included in ESI Figure S14). Selected CY3Z-NA samples with different morphology were analysed for its microstructures. As shown in Fig. 6a, a cubic-shape CY3Z-NA side view revealed similar filaments stacking in the z-direction as compared to CY6Z-NA sample shown in Fig. 6a. The adjacently deposited extrudate layers fused cleanly after sintering to form a solid dense structure. On top of simple cube structure, CY3Z-NA rectangular mesh of

various sizes with thick cross-hatching struts were also fabricated (Fig. 6b, c). The alternating deposition of the extrudate to form the cross-hatched structure was clearly observed from the SEM microstructure analysis. For each struts, two layers of extrudates were deposited, fusing into a single strut with diameter of approximately 1000  $\mu\text{m}$ . Mesh-like structures were still retained after sintering process without warping or developing drying cracks, even for meshes with relatively larger size (Fig. 6c). The comparison between the SEM images given in Figs. 5b, c, f and 6 suggested that similar grain size and grain size distributions were also obtained regardless of the sample morphologies, when samples were sintered at similar condition.

### Fabrication of partially stabilized zirconia: CY3Z-P

From the previous CY3Z-NA sintering study, a minimum sintering temperature of 1450 °C was required to obtain dense sample. In an attempt to reduce this sintering temperature, alternative commercial CY3Z-P powders (3 mol % yttria content and 0.25 wt%  $\text{Al}_2\text{O}_3$ ) with higher SSA (at  $9\text{ m}^2\text{ g}^{-1}$ ) than CY3Z-NA (at  $7\text{ m}^2\text{ g}^{-1}$ ) were employed as starting precursors. The sintering temperature influence towards the CY3Z-P microstructures was studied. The robocasted CY3Z-P cubic-shape green bodies were sintered at (1) 1400 °C and (2) 1500 °C for 5, 10 and 20 h, respectively. The SEM images of the sintered CY3Z-P samples' surface are summarized in Fig. 7a–f. The CY3Z-P microstructures suggested that sintering temperature as low as 1400 °C for 5 h was sufficient to obtain homogeneous and densely packed submicron-size grains of  $0.38 \pm 0.10\ \mu\text{m}$  with no observed surface porosity. At 1400 °C, the average grain sizes of sintered CY3Z-P samples were found to increase with sintering duration, at  $0.38 \pm 0.10$ ,  $0.46 \pm 0.13$  and  $0.56 \pm 0.16\ \mu\text{m}$  for 5, 10 and 20 h, respectively. The resultant grain size of CY3Z-P sample sintered at 1400 °C for 10 h ( $0.46 \pm 0.13\ \mu\text{m}$ ) was smaller than the grain size of CY3Z-NA sintered at similar condition ( $0.55 \pm 0.18\ \mu\text{m}$ ) without the presence of any surface porosity. Based on this result, YSZ powder with higher specific surface area has better sinterability.

The average CY3Z-P grain sizes were also found to increase with sintering temperature, with the average grain sizes of  $0.61 \pm 0.21$ ,  $0.84 \pm 0.27$  and



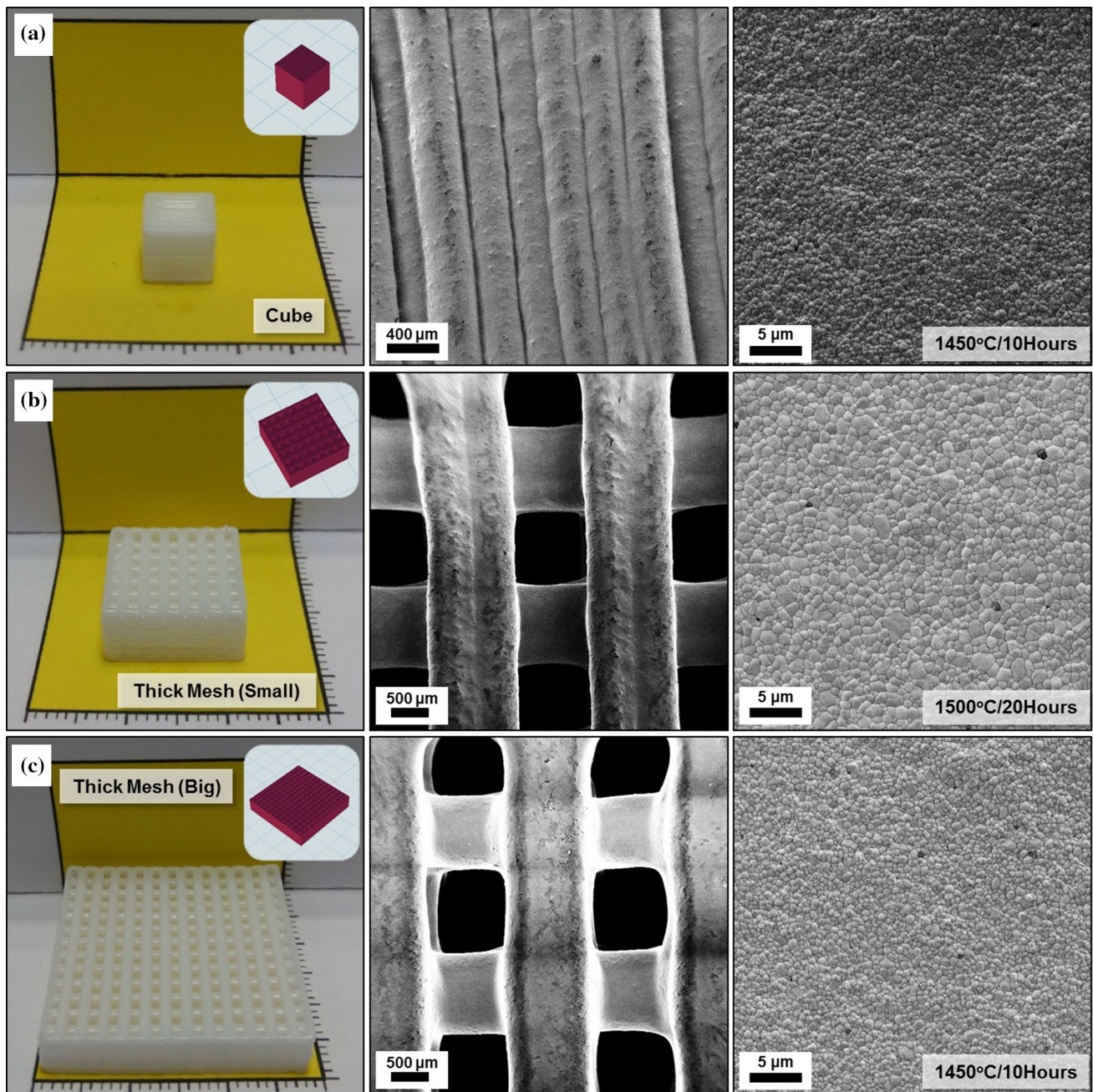


**Figure 6** Sintered CY3Z-NA structures: **a** cube, **b** rectangular mesh and **c** big rectangular mesh structures. From *left to right* photographs, low- and high-magnification SEM images (*inset* CAD model of respective sample).

$1.06 \pm 0.46 \mu\text{m}$  registered for CY3Z-P samples sintered at  $1500^\circ\text{C}$  for 5, 10 and 20 h, respectively. The comparison in Fig. 7g also showed a slight increase in the grain size distributions with increasing sintering temperature and duration. Due to the different formulations used for preparing CY3Z-P suspensions, relatively higher linear shrinkage of approximately 30–33% from the CAD dimension was observed for

CY3Z-P samples. Similar to CY6Z-NA and CY3Z-NA samples, secondary particles (darker contrast) were also present on the sintered CY3Z-P samples' surface. EDX elemental mapping were performed on one of the sintered CY3Z-P samples at  $1500^\circ\text{C}/10\text{ h}$  (see ESI Figure S15). From the mapping images, the darker particles in YSZ grain boundary indeed corresponded to the Al element which indicated the



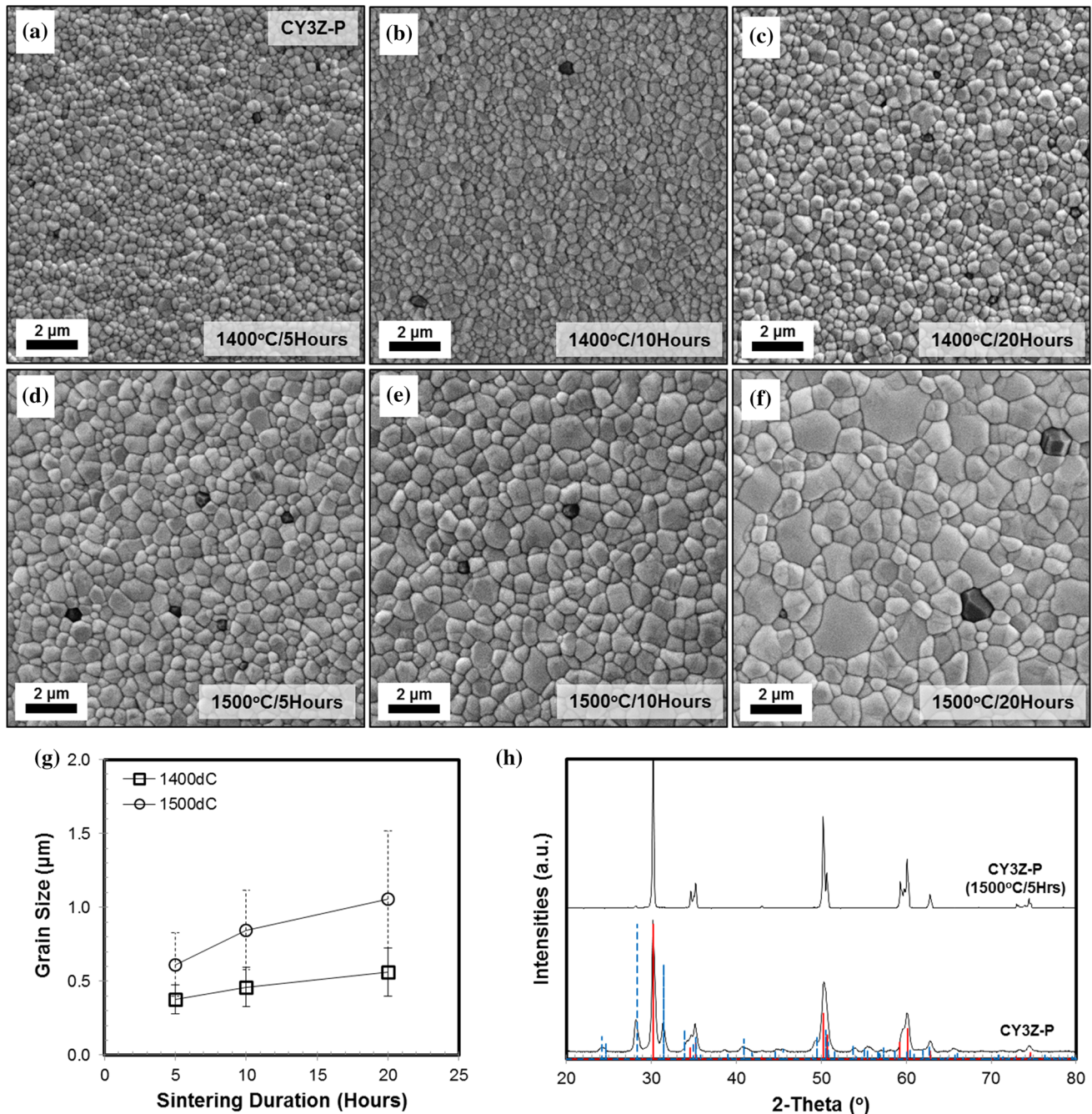


**Figure 7** SEM images of samples sintered at **a** 1400 °C/5 h, **b** 1400 °C/10 h, **c** 1400 °C/20 h, **d** 1500 °C/5 h, **e** 1500 °C/10 h and **f** 1500 °C/20 h. **g** Plot of the CY3Z-P grain sizes against the

presence of  $\text{Al}_2\text{O}_3$  inclusions on the grain boundary. No  $\text{Al}_2\text{O}_3$  particle was detected on the YSZ grain interior.

The crystalline phases of the sintered CY3Z-P samples were analysed by XRD. As shown in Fig. 7h, the diffraction peaks in the sintered CY3Z-P samples (1500 °C/5 h) XRD pattern were indexed against *t*-

sintering condition. **h** XRD patterns of CY3Z-P powders and sintered sample (1500 °C/5 h).

$\text{ZrO}_2$ . The minor *m*- $\text{ZrO}_2$  impurity phase that existed in the CY3Z-P powder precursor disappeared from the XRD patterns of sintered CY3Z-P (1500 °C/5 h). There was no additional phase presence in the *t*- $\text{ZrO}_2$  XRD pattern, suggesting the formation of tetragonal polycrystalline or partially stabilized zirconia structure without any additional impurity phases.

Additional XRD result for CY3Z-P sintered at 1500 °C for 10 and 20 h are given in Figure S16. Even at such prolonged sintering condition, *t*-ZrO<sub>2</sub> phase was retained without any *m*-ZrO<sub>2</sub> formation. XPS analysis was conducted for the CY3Z-P powders and sintered sample. The survey scan spectrum (Figure S11a) indicated the presence of C, Zr, Y, O and Al elements on both samples. The C 1s spectrum of both samples was fitted and assigned into their corresponding carbon atom components at different positions. Two C 1s peaks at 286.0 eV (C–O) and 288.2 eV (C=O) in CY3Z-P powder precursor diminished after high-temperature sintering due to complete binder burn-out. The original Zr 3d and Y 3d spectra of CY3Z-P powder (Figure S11c and Figure S11d) remained the same after sintering process, indicating that the chemical state and the tetragonal structure did not change after sintering. Similar to CY6Z-NA sample, the Al 2p peak at 74.2 eV (Figure S11f) in sintered CY3Z-P sample suggested the presence of sintering aid Al<sub>2</sub>O<sub>3</sub>. From the EDX elemental analysis on CY3Z-P powder precursor, no alumina was detected from CY3Z-P powder precursor. After sintering, the EDX elemental analysis revealed the presence of 1.28 wt% alumina in the surface of the sintered CY3Z-P (1500 °C/10 h).

Using the as-fabricated CY3Z-P suspensions, samples with simple and complex geometries such as cube, rectangular bar, coin, cylinder, monolith, hollow box, hexagon mesh and rectangular meshes of various sizes were fabricated. The photographs of sintered parts were included in ESI Figure S17. Selected CY3Z-P samples with different morphologies are presented in Fig. 8. In Fig. 8a, cube-shape CY3Z-P side view was examined by SEM. Similar with previous CY6Z-NA/CY3Z-NA observations, the adjacently deposited layers fused cleanly after sintering to form solid dense structure. Several small rectangular mesh structures with thin and thick struts and cross-hatch structure are also presented in Fig. 8b, c. Relatively large (Fig. 8d) and tall (Fig. 8e) hollow box structures were also successfully sintered. The side view of these structures showed a uniform stacking of extrudates in the z-direction. No porosity or extrudates overflowing due to continuous suspensions deposition was observed in the surface of such large structure. Lastly, large rectangular mesh green body (CAD dimension: 39 mm) was successfully sintered into 27-mm-wide mesh (Fig. 8f) with approximately 31% linear shrinkage. When

compared with CY3Z-NA mesh (Fig. 6c; sintered to 28 mm width at similar condition), the linear shrinkage for CY3Z-P sample was slightly higher. Such difference can be ascribed to the suspensions solid loading content, as indicated from the TGA analysis (Fig. 2d, e). Despite such shrinkage, mesh morphology was retained after sintering without warping or developing drying cracks.

### Density measurement and porosity analysis

The sintered CY6Z-NA, CY3Z-NA and CY3Z-P samples were sampled, and their density was evaluated by Archimedes principle. The YSZ green body was found to sinter successfully to more than 94% of the theoretical density (TD) of the bulk YSZ sample ( $\rho_{\text{bulk}} = 6.05 \text{ g cm}^{-3}$ ). The samples as-measured densities are plotted in Fig. 9a. For CY6Z-NA samples sintered at 1450, 1550 and 1600 °C (20 h), average measured density of 5.714, 5.752 and 5.915  $\text{g cm}^{-3}$  were obtained, respectively. These values corresponded to 94.5, 95.1 and 97.8% of the TD. Meanwhile, for CY3Z-NA samples sintered at 1450 °C for 10 h and 1500 °C for 20 h, average measured density of 5.801 and 5.857  $\text{g cm}^{-3}$  that corresponded to 95.9 and 96.8% TD was obtained. Lastly, the average measured density of CY3Z-P samples sintered at 1500 °C for 5, 10 and 20 h was found to be 5.787, 5.885 and 5.799  $\text{g cm}^{-3}$  which corresponded to 95.6, 97.3 and 95.8% TD.

Figure 9a suggests the presence of 3–6% of residual porosity within the sintered structures. While the variation of the specimen densities can be attributed to the possible printing variation from sample to sample, increasing sintering temperature or sintering time did not necessarily translate to significant increase in the sintered samples density. As the SEM images of CY6Z-NA (Fig. 3), CY3Z-NA (Fig. 5) and CY3Z-P (Fig. 7) samples did not show any presence of surface porosity, the residual porosity can be ascribed to the presence of closed pores within the sintered structure interior. Therefore, in order to visualize the internal structures of the bulk YSZ structures, neutron computed tomography (CT) imaging was performed on two sintered samples (with 16  $\mu\text{m}$  spatial resolutions): (1) CY6Z-NA (1500 °C/20 h) cube and (2) CY3Z-P (1500 °C/10 h) small rectangular mesh [40]. The resultant 3D images are summarized in Fig. 9b (CY6Z-NA; longitudinal section and 3D volume-rendered) and Fig. 9c, d



**Figure 8** Sintered CY3Z-P samples: **a** cube, **b** rectangular thin mesh, **c** rectangular mesh, **d** big hollow box, **e** tall hollow box, **f** big rectangular mesh and **g** hexagonal mesh structure. From *left to right* photographs, low- and high-magnification SEM images (*inset* CAD model of respective sample).

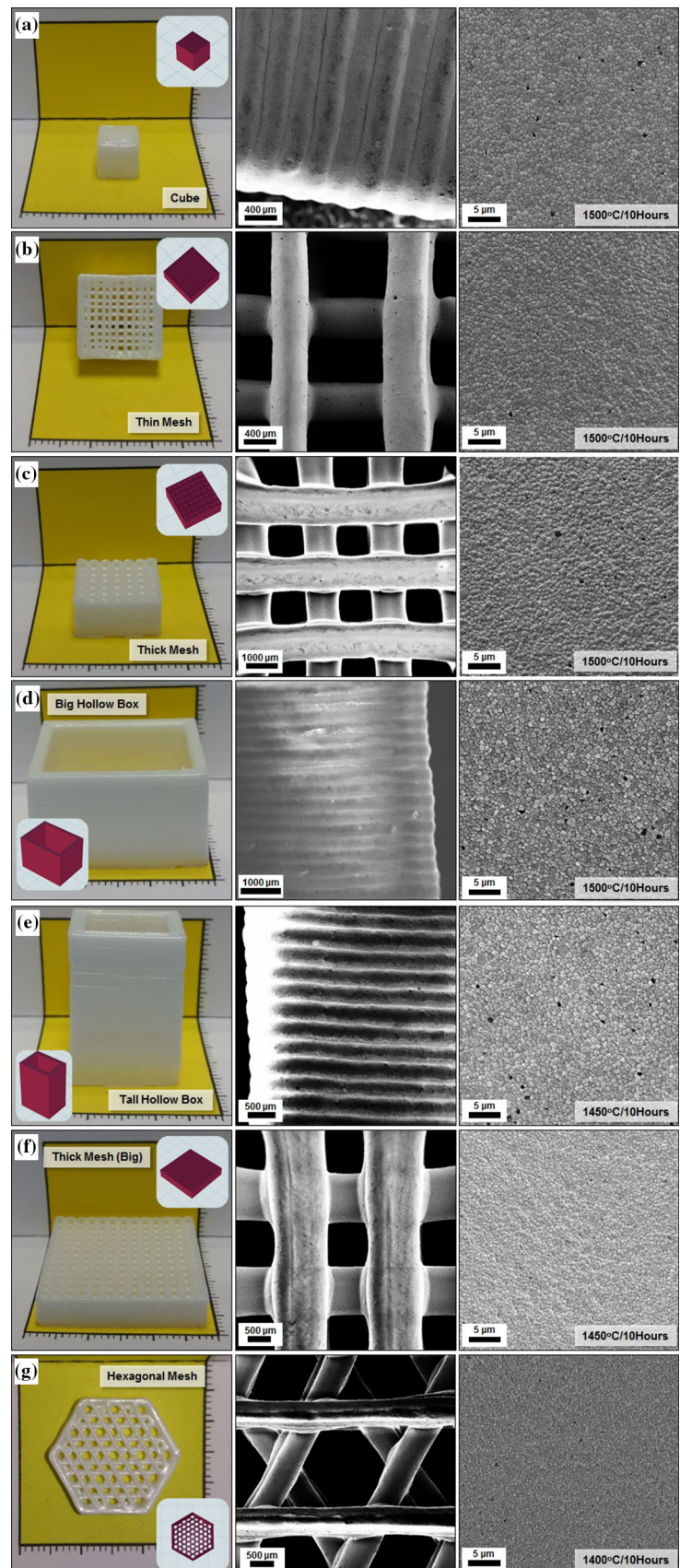
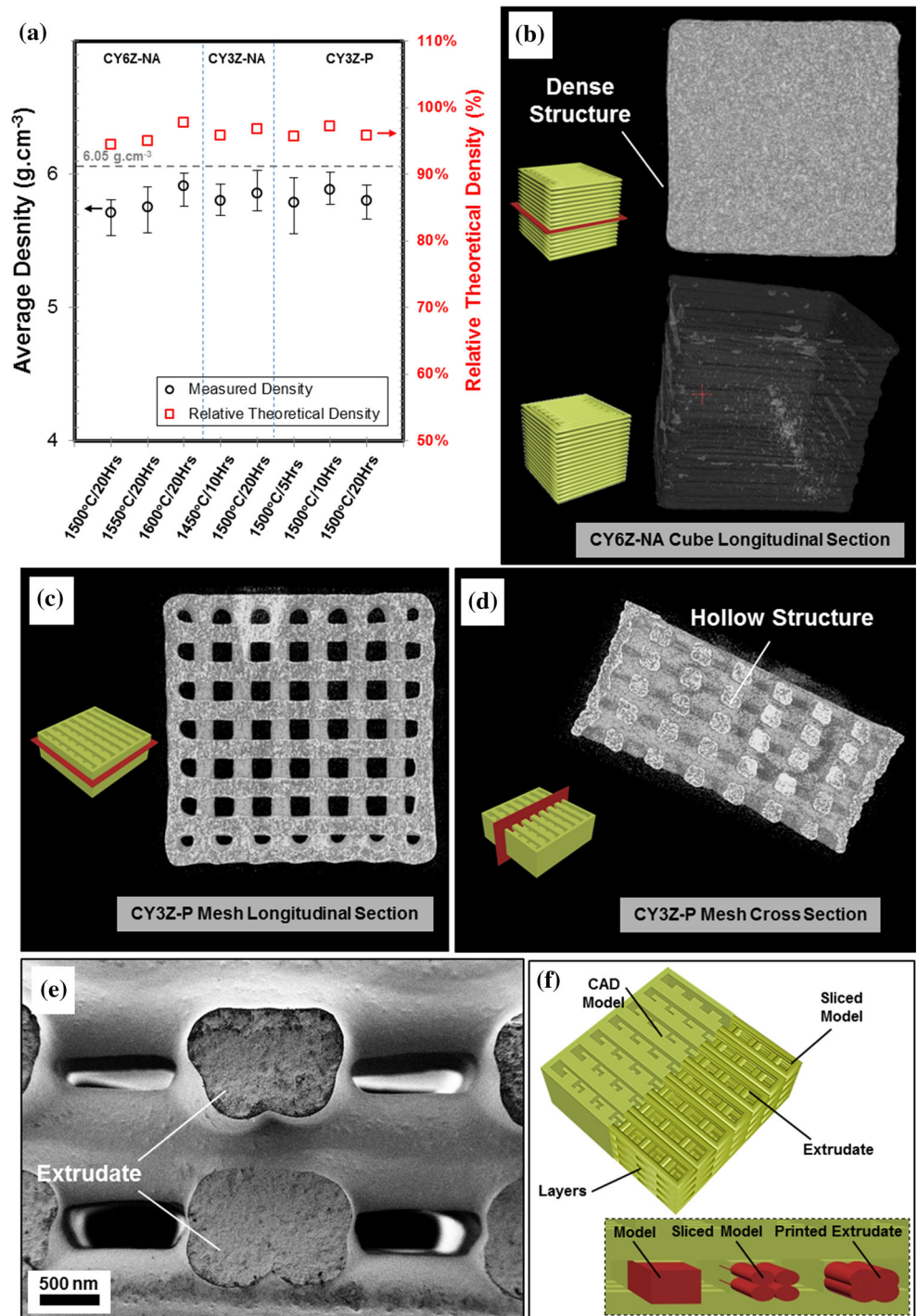




**Figure 9** a Plot of sintered YSZ density against the sintering conditions. Neutron imaging of the sintered YSZ samples: **b** longitudinal slice and volume rendered of solid CY6Z-NA cube (1500 °C/ 20 h; 100% infill), **c** longitudinal slice and **d** cross section of CY3Z-P mesh (1500 °C/10 h), **e** SEM image of the cross section of the CY3Z-P mesh (1400 °C/10 h), **f** Schematic illustrations of the rectangular mesh CAD model, and the printing profile showing the print head movement.



(CY3Z-P; cross section and longitudinal section). The CT images revealed that both CY6Z-NA cube and CY3Z-P mesh structure were sintered successfully and the shrinkage due to sintering process did not cause any internal macro-cracks formations. For the solid dense CY6Z-NA structure, defects or voids were found closer to the bottom region of the CY6Z-

NA cube, possibly due to the trapped air or oleic acid-releasing agent in the first few layers of the print. Inter-filament defects in the X–Y plane, parallel to the direction of the print head movement, were also observed (see Video S4 for more details). This can be also attributed to either slicing inaccuracy or trapped air bubbles during printing that resulted in

materials underfilling. Such defects will remain in the structure even after drying, debinding and sintering processes. Meanwhile, for the mesh CY3Z-P structures, the original hollow structure was still fully intact without any warping even with high linear shrinkage ( $\sim 33\%$ ) due to the sintering process. From Video S5, the sintered CY3Z-P mesh filament struts appeared to be well-aligned without any discontinuity. To further substantiate the CT imaging, CY3Z-P mesh was fractured and subsequently sintered at  $1400\text{ }^{\circ}\text{C}$  for 10 h. The cross-sectional SEM image (Fig. 9e) showed thick struts, each of which was formed by four extrudates. Based on this observation, the adjacently deposited extrudate fused cleanly with the subsequent layer extrudate to form a solid dense strut without leaving any macro-cavity in-between the extrudates as suggested by the schematic diagram given in Fig. 9f. Within the struts interior, micropores ( $<2\text{ }\mu\text{m}$ ) were observed. Both the macro-pores observed from CT image for CY6Z-NA and the micropores observed from SEM images contributed to the sintered samples porosity. These micropores were unable to be detected within the neutron imaging resolution. Overall, the neutron imaging analysis suggested that samples with complex internal hollow features can be readily printed using the robocasting process. Such structures can be useful to generate scaffolds for biomedical as well as catalytic applications [28, 48, 49].

### Mechanical testing: flexural strength and microhardness

The mechanical properties of the as-fabricated partially stabilized YSZ samples were determined from the three-point bending test and the microhardness test. All tests were performed without any surface finishing (i.e. grinding or polishing). CY3Z-P samples were selected for the tests due to its smaller grain size feature as compared to the CY3Z-NA sintered at similar condition. Two different testing bars (Fig. 10a, b) were fabricated: (1) with solid dense structure and (2) with mesh architectures (with 48.8 vol% macro-pores as estimated from the CAD model). The three-point bending test showed flexural strengths as high as  $216.3 \pm 18.3$  and  $242.8 \pm 11.4$  MPa for solid bar sintered at 1400 and 1500  $^{\circ}\text{C}$  for 10 h, respectively. Meanwhile, flexural strengths of  $57.3 \pm 5.2$  and  $57.2 \pm 6.8$  MPa were obtained for mesh samples sintered at 1400 and 1500  $^{\circ}\text{C}$ , respectively, for 10 h.

The flexural strength of the mesh samples was around 23–27% of the solid counterpart (Fig. 10c). The highest flexural strength obtained from the robocast samples reached only about 22.1% of the reported value for CY3Z-P (three-point bending test after compaction) [50]. To determine the failure origin that lead to the low flexural strength, the fractured surface after the three-point bending testing was examined under SEM. From the materials data sheet for CY3Z-P [50], the fracture toughness  $K_{1C}$  is  $6\text{ MPa m}^{1/2}$ . By using Griffith's equation for stress intensity factor  $K_C = \sigma\sqrt{\pi a}$ , the critical defects of the CY3Z-P specimen were calculated to be approximately  $\sim 194\text{ }\mu\text{m}$ . From the low-magnification SEM image of the fractured surface in Fig. 10b, the fracture origin was the surface flaw of the CY3Z-P specimen at the bottom region of the specimen (under tension during the three-point bending test). The surface flaw appeared to be rather sharp with crack length of more than  $200\text{ }\mu\text{m}$ . Such observation agreed well with Griffith criterion for the critical defect size. Therefore, the low flexural strength can be attributed to stress concentration at the tip of the surface defect. For the CY3Z-P specimen prepared by robocasting, the origin of defect of more than  $200\text{ }\mu\text{m}$  cannot be attributed to residual close pores after sintering. The defect was most likely the voids, either due to trapped air or oleic acid-releasing agent between filaments in the first layer of extrusion or due to under-extrusion of materials during robocasting that subsequently caused crack after sintering. The fractured surface from high-magnification SEM images given in Fig. 10a, b also showed a combination of both intergranular and transgranular fracture modes. Overall, there are few possible ways to reduce the stress magnification, inclusive of: (1) reducing the crack length through surface polishing, (2) decreasing the sharpness of the crack by further optimizing printing parameters and (3) reducing the amount of releasing agent applied to the printing substrate.

Lastly, microindentation test was also performed on the CY3Z-P mesh structures sintered at  $1400\text{ }^{\circ}\text{C}$  for 10 h (applied load of 49.03 N or 5kgf; HV05 indentation). The indentation profiles were included in Fig. 10d, e. The measured hardness of samples printed at  $5\text{ mm s}^{-1}$  (Fig. 10d) and  $20\text{ mm s}^{-1}$  (Fig. 10e) was 13.29 GPa (1355HV) and 12.28 GPa (1252HV), respectively. These values were comparable with the hardness reported for CY3Z-P by Vickers indentation (HV05) [50]. For both samples, no radial

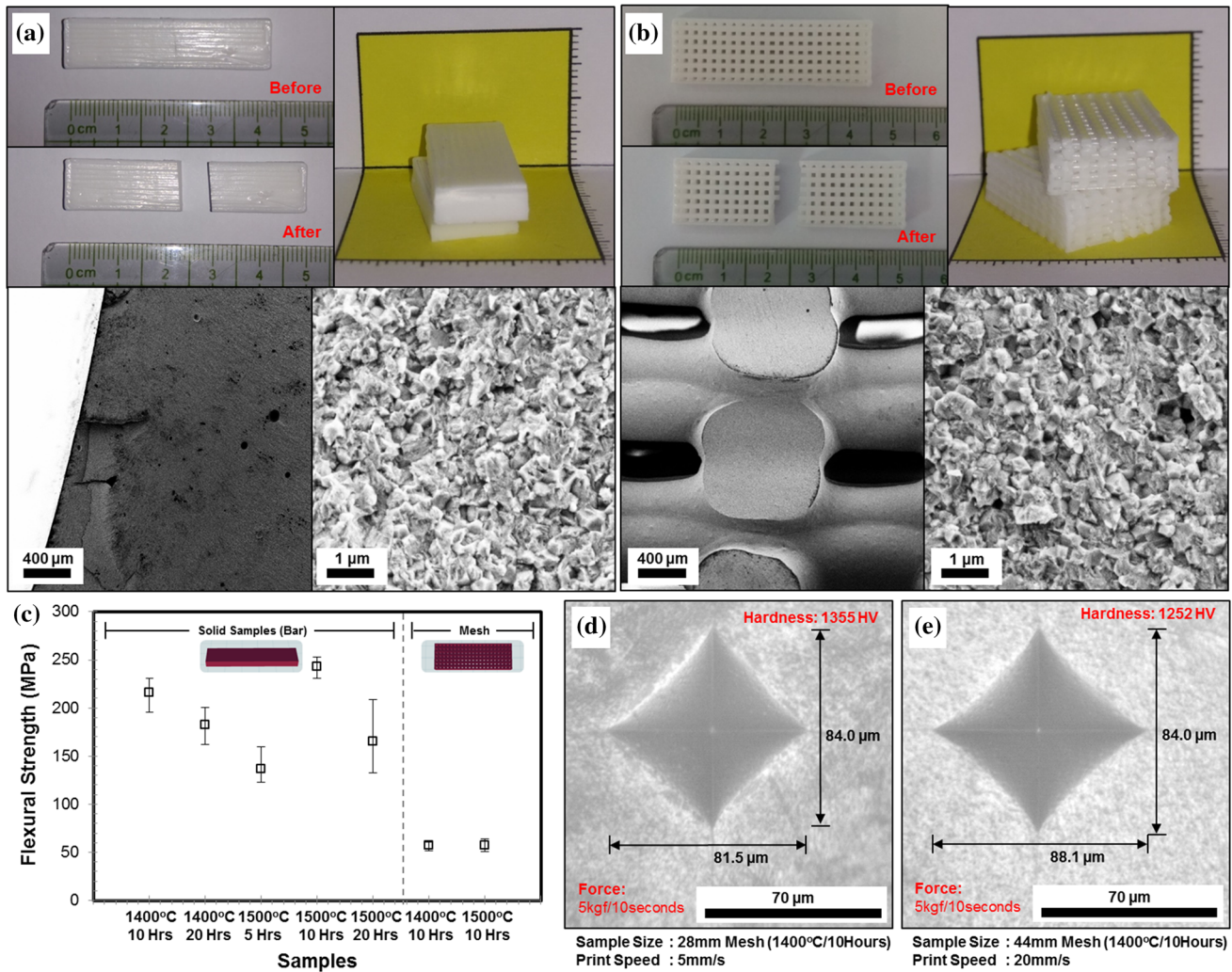


**Figure 10** Three-point bending test samples: **a** solid and **b** mesh structures (1500 °C/10 h). From left in clockwise direction: test specimen before and after bending test, fractured surface and SEM image of the fractured surface. **c** Plot of flexural strengths of

various CY3Z-P samples. Microindentation hardness test: optical images of the CY3Z-P mesh printed at **d** 5-mm s<sup>-1</sup> and **e** 20-mm s<sup>-1</sup> printing speeds.

crack was observed around the indented region. The hardness of the mesh printed at 20 mm s<sup>-1</sup> was found to be lower than the mesh printed at 5 mm s<sup>-1</sup>. This can be ascribed to the difference in extrudate surface roughness. When printed at slower speed, the deposited extrudate surface was smoother as compared to the samples printed at faster speed.

**Fabrication of large samples, repeatability and paste storage**

To demonstrate that YSZ suspensions fabricated in this work were suitable for robocasting process, three different aspects have to be fulfilled: (1) the ability to print larger structures with good sinterability (no

warping or deformation) at relatively short period of time, (2) the repeatability in fabricating similar objects and lastly, (3) the ability to print after long period of storage. The previous YSZ samples presented in Figs. 4, 6 and 8 were mostly robocasted at slow printing speed of 5 mm s<sup>-1</sup>. At such slow printing speed, it will take lengthy process in order to build a larger structure. To shorten the printing time, the printing speed has to be increased without compromising the print quality. Based on the previous rheological study, the YSZ suspension showed shear thinning behaviour up to 200 s<sup>-1</sup> shear rate. As such, the suspension was predicted to be compatible with higher printing speed up to 20–30 mm s<sup>-1</sup>. Figure 11a shows the still image of the 63-mm mesh green body



being printed at  $20 \text{ mm s}^{-1}$ . Figure 11b shows the resultant 63-mm mesh green body after drying, and Fig. 11c shows the sintered mesh. Despite the 30% linear shrinkage in  $X, Y$  direction (from 63 to 44 mm), the resultant sintered mesh still retained the original mesh morphology without developing any drying cracks, warping or deformation. The robocasting repeatability was demonstrated by fabricating (and sintering) mesh structures of various widths (CAD

dimension: 21, 39 and 63 mm) in multiple copies. As shown in Fig. 11d–f, identical mesh structures can be obtained straightforwardly. The mesh structures linear dimension did not vary significantly. Printing repeatability with CY3Z-NA and CY3Z-P samples were demonstrated in ESI Figure S18. Lastly, the prepared CY3Z-P suspension was also examined for its possible long-term storage. The as-fabricated CY3Z-P suspension was kept in a disposable syringe,

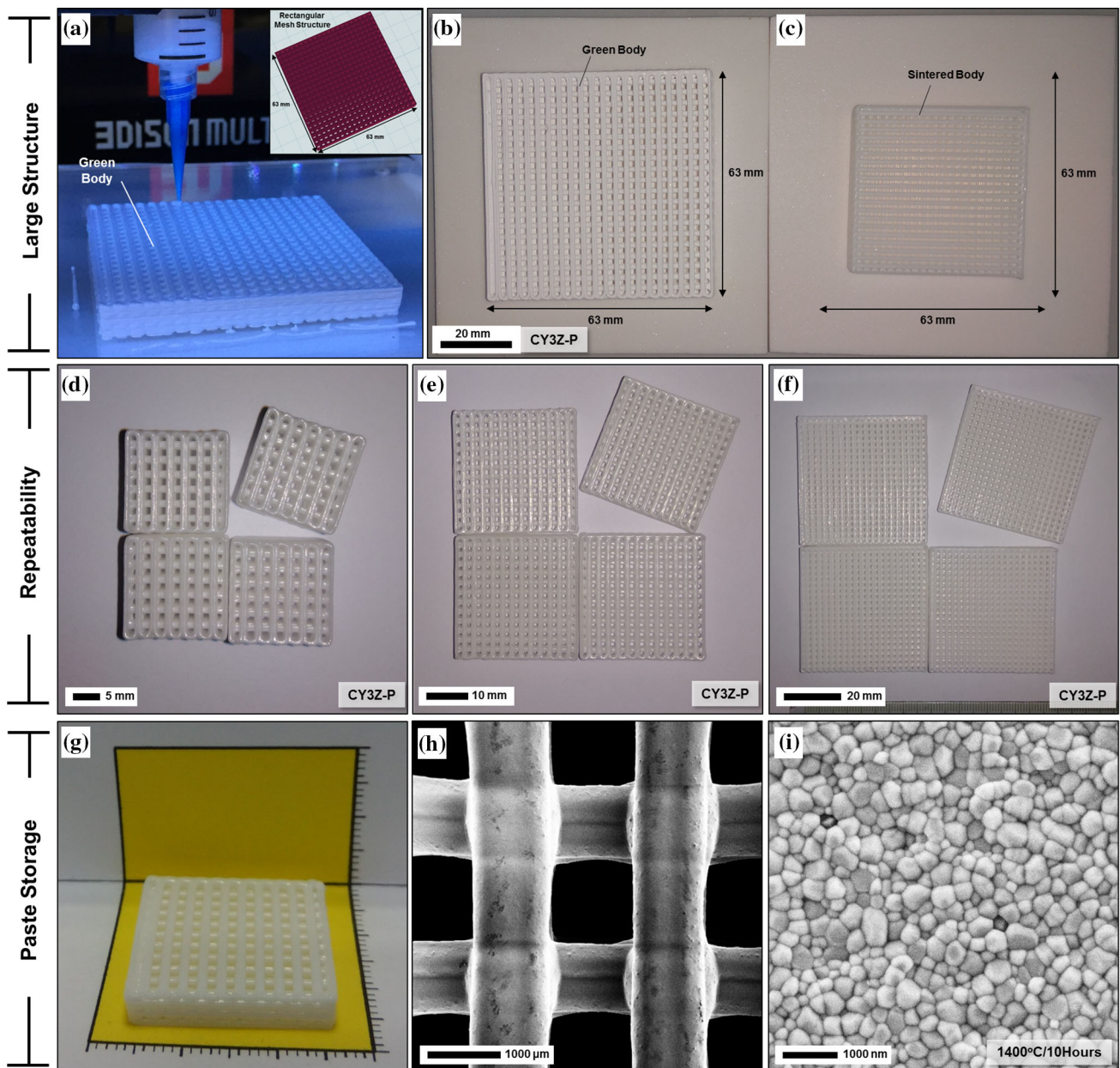


**Figure 11** Large structure fabrication: **a** Robocasting of large structures. 63-mm mesh: **b** after printing and **c** sintering ( $1400 \text{ }^\circ\text{C}/10 \text{ h}$ ). Repeatability: CY3Z-P mesh structures of various sizes:

**d** 21 mm, **e** 39 mm and **f** 63 mm. Paste Storage: **g** Sintered mesh structure ( $1400 \text{ }^\circ\text{C}/10 \text{ h}$ ) from 33-mm mesh green body fabricated using 7-day-aged paste and **h, i** its respective SEM images.

sealed with paraffin film and incubated at room temperature. After 7 days of ageing, the suspension was tested for its printability, and a simple 33-mm mesh green body was successfully fabricated at  $20 \text{ mm s}^{-1}$  and sintered at  $1400 \text{ }^\circ\text{C}$  (10 h) as shown in Fig. 11g. The SEM images of the sintered mesh are included in Fig. 11h, i. The resultant CY3Z-P average grain size was comparable with the previous results (Fig. 7b). Based on the present results, both fully and partially stabilized zirconia structures can be easily fabricated using robocasting method with good repeatability and the as-fabricated YSZ suspension can be stored prior to the printing.

## Conclusion

In summary, aqueous-based ceramic suspension containing commercial nano-sized YSZ powder with suitable rheology for ceramic robocasting was developed. In this work, suspension with low solid YSZ content ( $<38 \text{ vol}\%$ ) can be readily shaped into complex structure and sintered to dense part with  $>94\%$  of theoretical density while retaining its original morphology without any warping, crack or deformation despite the high linear shrinkage (up to 33%). Fully and partially stabilized YSZ samples can be obtained, depending on the starting precursors. Moreover, the microstructures analysis indicated that fully and partially stabilized YSZ with grain size as small as  $1.40 \pm 0.53$  (CY6Z-NA),  $0.59 \pm 0.18$  (CY3Z-NA) and  $0.38 \pm 0.10 \text{ }\mu\text{m}$  (CY3Z-P) can be achieved. Sintering temperature down to  $1400 \text{ }^\circ\text{C}$  can be attained with the use of higher specific surface area CY3Z-P precursor. The CY3Z-P samples exhibited flexural strengths up to  $242.8 \pm 11.4$  and  $57.3 \pm 5.2 \text{ MPa}$ , respectively, for solid and porous mesh (porosity of macro-pores  $>45\%$ ) samples with hardness up to 13.29 GPa. The developed YSZ suspension was demonstrated to be capable of fabricating large YSZ parts with good repeatability.

## Acknowledgements

The authors would like to thank Saint Gobain ZirPro for providing the zirconia powders. This project is financially supported by Saint Gobain (R-284-000-140-597), NUS Strategic Research Fund R-261-509-

001-646 and R-261-509-001-733 and NRF NRF-CRP16-2015-01 (R-284-000-159-281).

**Electronic supplementary material:** The online version of this article (doi:[10.1007/s10853-017-1491-x](https://doi.org/10.1007/s10853-017-1491-x)) contains supplementary material, which is available to authorized users.

## References

- [1] Belmonte M (2006) Advanced ceramic materials for high temperature applications. *Adv Eng Mater* 8(8):693–703
- [2] Kelly JR, Denry I (2008) Stabilized zirconia as a structural ceramic: an overview. *Dent Mater* 24(3):289–298
- [3] Gautam C, Joyner J, Gautam A, Rao J, Vajtai R (2016) Zirconia based dental ceramics: structure, mechanical properties, biocompatibility and applications. *Dalton Trans* 45(48):19194–19215
- [4] Park J-S, Kim H, Kim I-D (2014) Overview of electroceramic materials for oxide semiconductor thin film transistors. *J Electroceram* 32(2):117–140
- [5] Schlordt T, Schwanke S, Keppner F, Fey T, Travitzky N, Greil P (2013) Robocasting of alumina hollow filament lattice structures. *J Eur Ceram Soc* 33(15–16):3243–3248
- [6] Manicone PF, Rossi Iommetti P, Raffaelli L (2007) An overview of zirconia ceramics: basic properties and clinical applications. *J Dent* 35(11):819–826
- [7] Zhao S, Xiao W, Rahaman MN, O'Brien D, Seitz-Sampson JW, Sonny Bal B (2017) Robocasting of silicon nitride with controllable shape and architecture for biomedical applications. *Int J Appl Ceram Technol* 14(2):117–127
- [8] Cai K, Román-Manso B, Smay JE, Zhou J, Osendi MI, Belmonte M, Miranzo P (2012) Geometrically complex silicon carbide structures fabricated by robocasting. *J Am Ceram Soc* 95(8):2660–2666
- [9] Chen Z, Song X, Lei L, Chen X, Fei C, Chiu CT, Qian X, Ma T, Yang Y, Shung K, Chen Y, Zhou Q (2016) 3D printing of piezoelectric element for energy focusing and ultrasonic sensing. *Nano Energy* 27:78–86
- [10] Tuttle BA, Smay JE, Cesarano J, Voigt JA, Scofield TW, Olson WR, Lewis JA (2001) Robocast  $\text{Pb}(\text{Zr}_{0.95}\text{Ti}_{0.05})\text{O}_3$  ceramic monoliths and composites. *J Am Ceram Soc* 84(4):872–874
- [11] Jakus AE, Taylor SL, Geisendorfer NR, Dunand DC, Shah RN (2015) Metallic architectures from 3D-printed powder-based liquid inks. *Adv Func Mater* 25(45):6985–6995
- [12] Wei X, Nagarajan RS, Peng E, Xue J, Wang J, Ding J (2016) Fabrication of  $\text{YBa}_2\text{Cu}_3\text{O}_{7-x}$  (YBCO) superconductor bulk

- structures by extrusion freeforming. *Ceram Int* 42(14): 15836–15842
- [13] Tsampas MN, Sapountzi FM, Vernoux P (2015) Applications of yttria stabilized zirconia (YSZ) in catalysis. *Catal Sci Technol* 5(11):4884–4900
- [14] Devi PS, Sharma AD, Maiti HS (2004) Solid oxide fuel cell materials: a review. *Trans Indian Ceram Soc* 63(2):75–98
- [15] Porter DL, Evans AG, Heuer AH (1979) Transformation-toughening in partially-stabilized zirconia (PSZ). *Acta Metall* 27(10):1649–1654
- [16] Durá OJ, López de la Torre MA, Vázquez L, Chaboy J, Boada R, Rivera-Calzada A, Santamaria J, Leon C (2010) Ionic conductivity of nanocrystalline yttria-stabilized zirconia: grain boundary and size effects. *Phys Rev B* 81(18): 184301
- [17] Shanti NO, Hovis DB, Seitz ME, Montgomery JK, Baskin DM, Faber KT (2009) Ceramic laminates by gelcasting. *Int J Appl Ceram Technol* 6(5):593–606
- [18] Hotza D, Greil P (1995) Review: aqueous tape casting of ceramic powders. *Mater Sci Eng A* 202(1):206–217
- [19] Mohd Foudzi F, Muhamad N, Bakar Sulong A, Zakaria H (2013) Yttria stabilized zirconia formed by micro ceramic injection molding: rheological properties and debinding effects on the sintered part. *Ceram Int* 39(3):2665–2674
- [20] Lewis JA, Smay JE, Stuecker J, Cesarano J (2006) Direct ink writing of three-dimensional ceramic structures. *J Am Ceram Soc* 89(12):3599–3609
- [21] Travitzky N, Bonet A, Dermeik B, Fey T, Filbert-Demut I, Schlier L, Schlordt T, Greil P (2014) Additive manufacturing of ceramic-based materials. *Adv Eng Mater* 16(6):729–754
- [22] Zocca A, Colombo P, Gomes CM, Günster J (2015) Additive manufacturing of ceramics: issues, potentialities, and opportunities. *J Am Ceram Soc* 98(7):1983–2001
- [23] Qian B, Shen Z (2013) Laser sintering of ceramics. *J Asian Ceram Soc* 1(4):315–321
- [24] Manogharan G, Kioko M, Linkous C (2015) Binder jetting: a novel solid oxide fuel-cell fabrication process and evaluation. *JOM* 67(3):660–667
- [25] Halloran JW (2016) Ceramic stereolithography: additive manufacturing for ceramics by photopolymerization. *Annu Rev Mater Res* 46(1):19–40
- [26] Allahverdi M, Danforth SC, Jafari M, Safari A (2001) Processing of advanced electroceramic components by fused deposition technique. *J Eur Ceram Soc* 21(10–11): 1485–1490
- [27] Lu X, Lee Y, Yang S, Hao Y, Evans JRG, Parini CG (2009) Fine lattice structures fabricated by extrusion freeforming: process variables. *J Mater Process Technol* 209(10): 4654–4661
- [28] Maazouz Y, Montufar EB, Guillem-Marti J, Fleps I, Ohman C, Persson C, Ginebra MP (2014) Robocasting of biomimetic hydroxyapatite scaffolds using self-setting inks. *J Mater Chem B* 2(33):5378–5386
- [29] Mason MS, Huang T, Landers RG, Leu MC, Hilmas GE (2009) Aqueous-based extrusion of high solids loading ceramic pastes: process modeling and control. *J Mater Process Technol* 209(6):2946–2957
- [30] Scheithauer U, Schwarzer E, Richter H-J, Moritz T (2015) Thermoplastic 3D printing—an additive manufacturing method for producing dense ceramics. *Int J Appl Ceram Technol* 12(1):26–31
- [31] Vaidyanathan R, Walish J, Lombardi JL, Kasichainula S, Calvert P, Cooper KC (2000) The extrusion freeforming of functional ceramic prototypes. *JOM* 52(12):34–37
- [32] Leu MC, Deuser BK, Tang L, Landers RG, Hilmas GE, Watts JL (2012) Freeze-form extrusion fabrication of functionally graded materials. *CIRP Ann Manuf Technol* 61(1):223–226
- [33] de Hazan Y, Thänert M, Trunec M, Misak J (2012) Robotic deposition of 3d nanocomposite and ceramic fiber architectures via UV curable colloidal inks. *J Eur Ceram Soc* 32(6):1187–1198
- [34] Faes M, Valkenaers H, Vogeler F, Vleugels J, Ferraris E (2015) Extrusion-based 3D printing of ceramic components. *Procedia CIRP* 28:76–81
- [35] Feilden E, Blanca EG-T, Giuliani F, Saiz E, Vandeperre L (2016) Robocasting of structural ceramic parts with hydrogel inks. *J Eur Ceram Soc* 36(10):2525–2533
- [36] Lu X, Lee Y, Yang S, Hao Y, Uvic R, Evans JRG, Parini CG (2008) Fabrication of electromagnetic crystals by extrusion freeforming. *Metamaterials* 2(1):36–44
- [37] Lu X, Lee Y, Yang S, Hao Y, Evans JRG, Parini CG (2010) Solvent-based paste extrusion solid freeforming. *J Eur Ceram Soc* 30(1):1–10
- [38] Michna S, Wu W, Lewis JA (2005) Concentrated hydroxyapatite inks for direct-write assembly of 3-D periodic scaffolds. *Biomaterials* 26(28):5632–5639
- [39] Smay JE, Cesarano J, Lewis JA (2002) Colloidal inks for directed assembly of 3-D periodic structures. *Langmuir* 18(14):5429–5437
- [40] Garbe U, Randall T, Hughes C (2011) The new neutron radiography/tomography/imaging station DINGO at OPAL. *Nucl Instrum Methods Phys Res Sect A* 651(1):42–46
- [41] Lewis JA (2000) Colloidal processing of ceramics. *J Am Ceram Soc* 83(10):2341–2359
- [42] Moreno R (2012) Colloidal processing of ceramics and composites. *Adv Appl Ceram* 111(5-6):246–253



- [43] Hidber PC, Graule TJ, Gauckler LJ (1996) Citric acid—a dispersant for aqueous alumina suspensions. *J Am Ceram Soc* 79(7):1857–1867
- [44] Çınar S, Akinc M (2014) Ascorbic acid as a dispersant for concentrated alumina nanopowder suspensions. *J Eur Ceram Soc* 34(8):1997–2004
- [45] Stuecker JN, Cesarano Iii J, Hirschfeld DA (2003) Control of the viscous behavior of highly concentrated mullite suspensions for robocasting. *J Mater Process Technol* 142(2): 318–325
- [46] Tekeli S (2007) The solid solubility limit of  $\text{Al}_2\text{O}_3$  and its effect on densification and microstructural evolution in cubic-zirconia used as an electrolyte for solid oxide fuel cell. *Mater Des* 28(2):713–716
- [47] Tekeli S, Demir U (2005) Colloidal processing, sintering and static grain growth behaviour of alumina-doped cubic zirconia. *Ceram Int* 31(7):973–980
- [48] Houmard M, Fu Q, Genet M, Saiz E, Tomsia AP (2013) On the structural, mechanical, and biodegradation properties of HA/ $\beta$ -TCP robocast scaffolds. *J Biomed Mater Res B Appl Biomater* 101(7):1233–1242
- [49] Michorczyk P, Hedrzak E, Wegrzyniak A (2016) Preparation of monolithic catalysts using 3D printed templates for oxidative coupling of methane. *J Mater Chem A* 4(48): 18753–18756
- [50] Saint Gobain. ZirPro CY3Z-P Technical Data Sheet. <http://www.zirpro.com/zirconia-beads-powders/yttria-stabilized-zirconia>